BACKSIDE-CONFIGURED PLASMONIC STRUCTURE FOR

QUANTUM DOT INFRARED PHOTODETECTOR

ENHANCEMNET

BY

GUIRU GU

SUBMITTED IN PARTIAL FULFILLMENT OF THE REQUIREMENTS
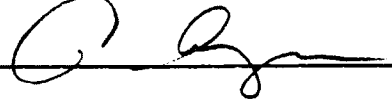
FOR THE DEGREE OF DOCTORAL OF PHILOSOPHY
ELECTRICAL AND COMPUTER ENGINEERING
UNIVERSITY OF MASACHUSETTS LOWELL

Signature of Author: _____ **Date:** _7/22/2013_

Signature of Thesis Supervisor: _____

Name Typed: _____Xuejun Lu_____

Signatures of Other Thesis Committee Members:

Committee Member Signature: _____

Name Typed: _____Alkim Akyurtlu_____

Committee Member Signature: _____

Name Typed: _____Christopher P. McCarroll_____

UMI Number: 3574005

UMI

Dissertation Publishing

UMI 3574005

ProQuest

BACKSIDE-CONFIGURED PLASMONIC STRUCTURE FOR QUANTUM DOT INFRARED PHOTODETECTOR ENHANCEMNET

BY

GUIRU GU

ABSTRACT OF A DISSERTATION SUBMITTED TO THE FACULTY OF THE
DEPARTMENT OF ELECTRICAL AND COMPUTER ENGINEERING
IN PARTIAL FULFILLMENT OF THE REQUIREMENTS

FOR THE DEGREE OF
DOCTORAL OF PHILOSOPHY
ELECTRICAL AND COMPUTER ENGINEERING
UNIVERSITY OF MASACHUSETTS LOWELL
2013

Dissertation Supervisor: Xuejun Lu. Ph.D.
Professor, Department of Electrical and Computer Engineering

Abstract

Since infrared light was discovered in 1800, infrared detection has gradually grown into one of cornerstones in the modern science and technology. InAs/GaAs quantum dot infrared photodetectors (QDIPs) have emerged as a promising technology for infrared detection due to the advantages such as normal incident detection, low dark current, high photoconductive (PC) gain, and etc. However, the total number of quantum dots (QD) layers is limited by the accumulation of strain and the strain induced defects and dislocations, therefore, the total percentage of light that can be absorbed in the active region is limited. Accordingly, the QDIP detectivity is still low. Surface plasmon resonance (SPR), predicted by Ritchie in 1957, offers an effective surface light trapping and enhancement technique, which provides a promising solution to overcome the major limitation of the thin active QD region issue in QDIPs.

Tremendous of work has been established in our research group to validate the understanding of the SPR enhancement for the QDIPs, and take further steps in investigating the parameters of the plasmonic structure like the periods, hole diameters and metal thickness.

In this work, I am going to report a quantum dot infrared photodetector (QDIP) enhanced by a backside-configured surface plasmonic structure with an over 40 times peak photocurrent enhancement. The QDIP enhancement by the backside-configure plasmonic structure is compared with that by the top-configured plasmonic structure. The backside configured plasmonic structure shows much higher photocurrent and photodetectivity D^* enhancement.

And further analysis of the excitation of the surface plasmonic waves by the backside-configured and top-configured plasmonic structures is made. The higher enhancement is attributed to the more efficient surface plasmonic excitation by the backside-configured plasmonic structure.

In addition, further investigation on the relationship of the plasmonic loss and the device performance enhancement is studied. Other backside configured plasmonic structures such as the localized plasmonic surface plasmonic resonance (LSPR) is also investigated and compared with the propagation SPR.

ACKNOWLEDGEMENT

TABLE OF CONTENTS

LIST OF FIGURES

CHAPTER I INTRODUCTION OF INFRARED TECHNOLOGY

1.1 Background

Infrared light was discovered in 1800 by William Herschel[1] and since then infrared detection has gradually developed as cornerstones in the modern history of science and technology. Its popularity originated from the fact that it provides us to see when visible light does not allow to, which is also known as "night vision", or frequently depicted as infrared imaging. What's more, infrared detectors are crucial for an abundance of other applications.

First, infrared emitters and detectors are actually extensively used in our daily life, such as the remote controls of TV, radio, DVD player, and video game consoles. Infrared sensors and cameras are successfully used to detect motion in XBOX Kinect video games. This is probably the most common and widespread use of commercial infrared technology.

Infrared imaging makes use of electromagnetic radiation emitted from any object, whose absolute temperature and surface emissivity collectively determine the wavelengths of the radiation. Therefore, even small changes of temperatures on the object can be reflected as variations in the emission spectra, which bring infrared cameras into widespread use of industry. For example, infrared thermography inspection can be utilized to detect "hot-spots" on power transmission lines, or to identify intruders in low visibility, or to detect

manufacturing flaws on the machine. Figure 1 below shows the visible and infrared images (Image source: http://www.spitzer.caltech.edu).

Figure 1, Visible and IR image (http://spitzer.caltech.edu)

Regarding as recent world events, such as the terrorist attacks of 9/11 and the Boston Marathon Bombing, specific molecular recognition method based on chemical sensing technology is becoming very critical, wherein certain molecules will resonate at specific frequencies while being stimulated by infrared radiation[2]. Accordingly, a number of chemical and biological detection systems have been developed[3]. By doing so, the safety of civilian populations can be enhanced. Fig 2 below shows the IR absorption spectrum (image from http://rebar.ecn.purdue.edu).

2
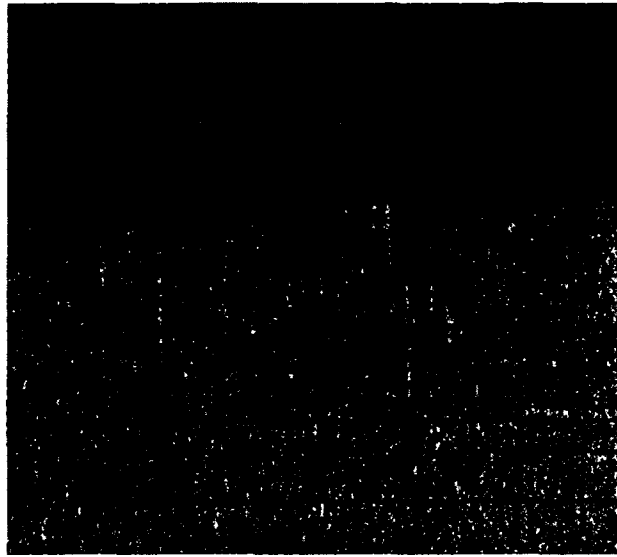
Figure 2, IR absorption spectrum of some chemical gases. (image from http://rebar.ecn.purdue.edu).

Infrared sensors and detectors can be used to monitor blood flow[4] in the medical field, by use of which diagnoses on cancer cells and circulatory diseases can be performed more accurately and more quickly. Moreover, infrared sensors can be used to distinguish the proper skin sites from those burned ones to help enhance survival rates.

Ultra long wavelength infrared detectors form a key building block for numerous earth remote sensing, space and planetary exploration applications, especially those require long-range sensing and trace element detections. For example, the weather satellites equipped with infrared imaging system can monitor the atmospheric properties such as temperature and winds, planetary exploitations such as trace constituents, mineral identification, and even vegetation mapping. The main advantage of infrared technology lies in that images can be produced at night, allowing a continuous sequence of weather study. Finally, infrared detectors are useful in astronomy applications. Since the stars are usually very far apart and relatively at

low temperature, the infrared detection and imaging capability with extremely low power consumption will provide an enabling telescope for the space exploration.

Infrared properties such as night vision, target designation and long-range missile detection are extensively used in military applications. Helmet instrumented with night vision functionality allow soldiers to operate missions in total darkness. Moreover, illumination of the target can be scanned by infrared detectors on laser spots, which makes jet flights or missiles traceable and thus early warning can be provided by satellite or ground-based infrared detectors. Figure 3 shows one of the applications of infrared detectors in military use (Image from: http://rst.gsfc.nasa.gov).

Figure 3, Infrared detector application in military (Image from: http://rst.gsfc.nasa.gov)

Infrared sensors and detectors have reached out to more corners of our society than expected, as mentioned before like the military targeting and tracking, law enforcement, medical diagnose, space science, electronics and even arts. Apparently, taking a deep dive of the mechanism and properties of infrared detectors will be more beneficial to its future

application. In the next sections. two distinctive types of infrared detectors, "Thermal detectors" and "Photo detectors", will be discussed in detail.

1.2 Infrared detectors

Two distinctive groups can be distinguished in terms of the detection of infrared light: (1) thermal detectors, such as microbolometers [5], pyroelectric detectors; and (2) photodetectors such as HgCdTe [6, 7], InAsSb–InSb[8, 9], quantum well infrared photodetectors (QWIPs) [10-12], and quantum dots infrared detectors (QDIPs)[13, 14]. Thermal detectors exhibit more or less change in the basic physical properties of the material after being exposed to the infrared light. While, photodetectors are mainly based on the carrier transitions in different bands like the impurity band, interband and intersubband after absorbing the infrared light, which will generate the photocurrents.

1.2.1 Thermal detector

The thermal detector always requires its material to be strongly temperature-dependent. And these kind of thermal-type devices can absorb photons thoroughly or with a wide. flat response function of wavelength, which results in the fact that thermal detectors always own a larger bandwidth with respect to the photodetectors. Finally, the thermal detectors are readily available in commercial because they are less expensive than photodetectors, and they offer uncooled operation. which means that they are more portable for field applications. However, thermal detectors are usually based on thermal-induced effects (resistance, polarization or

5

beam deflection). Such thermal process makes thermal detectors intrinsically slow in response

(> 4ms). The slow response time would limit the temporal resolution of a thermal IR sensor

and make it unsuitable for high-speed applications such as real time chemical detection and

identification and display. In addition, thermal detectors have limited sensitivity, which

constrain their applications in low level chemical sensing and detection. Last but not least,

they are not able to integrate two-color based detection into one device, which is normally

accepted as a requirement of high resolution in imaging. Eventually, photon detectors are

more widely preferred than thermal detectors.

1.2.2 Photodetector

Photodetectors are based on photon excited electron generation process. Such

photo-electric processes are intrinsically highly sensitive and fast. As a result, photodetectors

and imaging arrays can offer high sensitivity and real time detection. However, the photon

detectors have a limitation that the detecting units requires to be cooled, in another word, the

detectors need to be equipped with cooling system. Since the energy of infrared light is so tiny

that it can be influenced by the signal generated from the dark current at higher temperatures.

There are basically three types of photodetcetors: mercury cadmium telluride detectors,

quantum well infrared photodetectors, and quantum dot infrared photodetectors. The

advantages and disadvantages of these three types of photon detectors are discussed below.

    a. Bulk material photodetector

Current state-of-the arts IR photodetecting technology is based on low bandgap materials, such as HgCdTe and InAsSb–InSb. Mercury cadmium telluride detectors are intrinsic, bulk material detector, which detector IR light by interband transitions as shown in Figure 4. While tremendous advances have been made in the photodetecting technology, the existing photodetectors need to be cooled down to below 80 K to reduce the detector noise. The requirement for cryogenic cooling systems adds cost, power consumption, weight and reliability issues, thereby making it unsuitable for standoff sensing and detections. There are some other drawbacks to this technology like the difficulties in growing and processing, the nonuniform dopant incorporation.
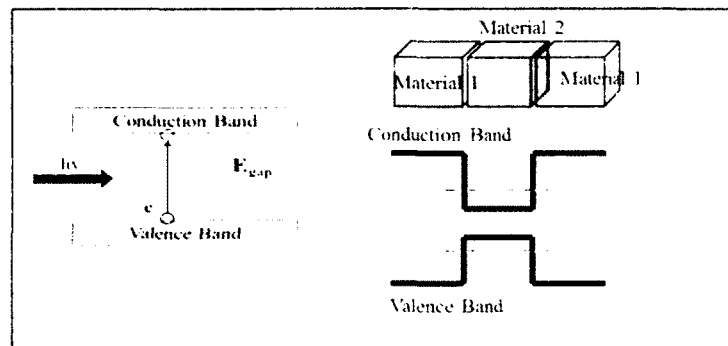
Figure 4, Schematic structure of interband transition of bulk material photodetector

b. Quantum Well photodetector

The GaAs/AlGaAs quantum well infrared photo-detector (QWIP) is an alternative technology that can detect infrared light generated by intersubband transitions in the conduction band. The schematic structure, density states and the detection mechanism of the QWIP are shown in Figure 5. The QWIP has a lot of advantages, such as low cost, good

uniformity, high sensitivity with wave length flexibility and so on. Its main disadvantage lies

in that it's not able to detect normally incident light, therefore, not all incident photons in the

growth direction can be absorbed according to the quantum selection rules. Accordingly,

coupling gratings are necessary for QWIP photodetectors.
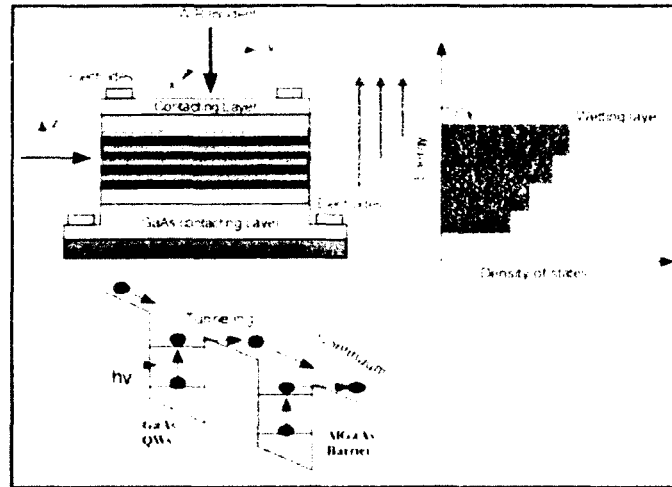
Figure 5, The schematic structure of the QWIP, the density states of the QDs and the detection mechanism of the QWIP

c. Quantum dots photodetector

The InAs/GaAs quantum dot infrared photodetectors (QDIPs) are based on intersubband

transitions in self-assembled InAs quantum dots (QDs). The schematic of the QDIPs and QDs

and the detection mechanism are shown in Figure. 6. When the incident light shines on the

detectors, electrons from confined state in the conduction band will absorb certain photon

energies, and get excited to a higher energy level near continuum band. With some applied

voltage bias, electrons will tunnel through potential barriers to the continuum band, and then

get collected as photocurrent.

8
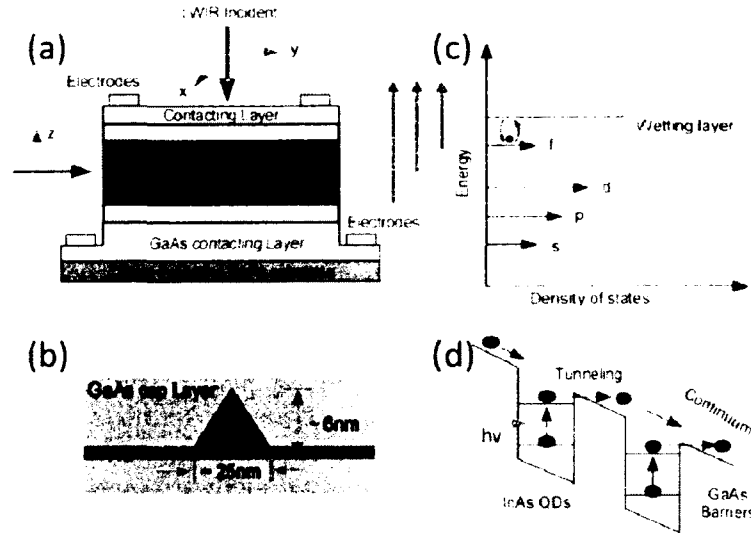
Figure 6, (a) The schematic structure of the QDIP; (b) the schematic structure of the QD; (c) the density states of the QDs and (d) the detection mechanism of the QDIP

InAs/GaAs quantum dot infrared photodetectors (QDIPs) based on intersubband transitions in self-assembled InAs quantum dots (QDs) have emerged as a promising technology due to the advantages as listed:

(1) Normal incidence

Provided by the three-dimensional (3D) quantum confinement of carriers, the QDIPs are sensitive to normal incident radiation [15]. The normal incidence detection capability greatly simplifies the fabrication complexity for a large format (1K×1K) focal plane array (FPA). Figure 7 shows the FPA chips made in our research group and the infrared images by the FPAs.
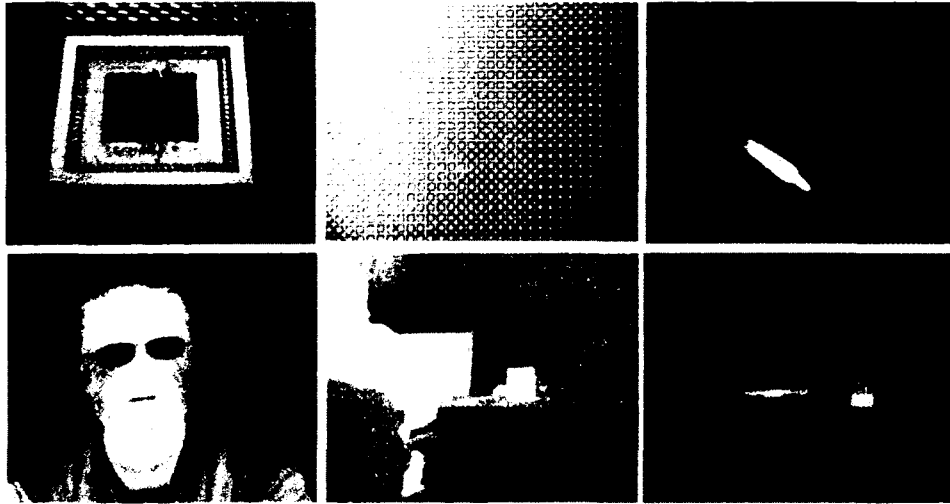
Figure 7, FPA chips in our group and the infrared images by the FPA in our lab

(2) Low dark current

Compared with quantum well (QW) based infrared photodetectors, QDIP also shows lower dark current [15-17] due to the 3D quantum confinement. Figure 8 shows the dark current of various materials as temperature dependence[16] and Figure 9 illustrates the dark current densities of LWIR QDIPs developed by Applied NanoFemto technologies (ANFT) compare to QWIPs which shows that QDIPs has over 10^2 times less dark current than QWIPs[17]. Both figures clearly present that the QDIP photodetectors have very low dark current.
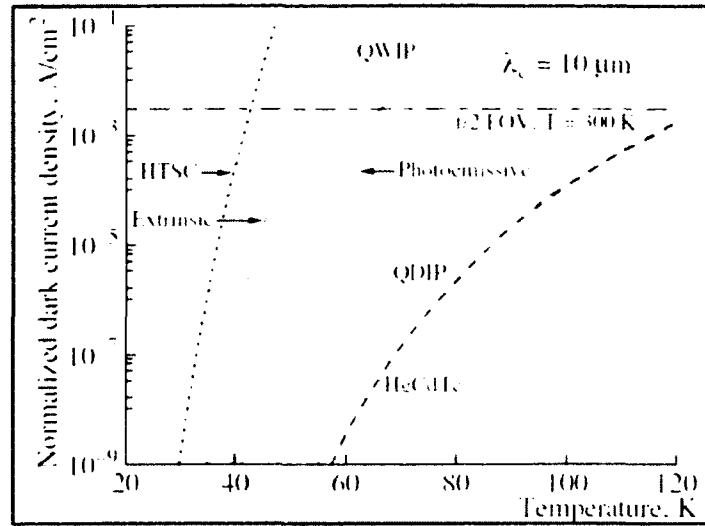
Figure 8, Different material dark current density comparison with temperature dependence[16].
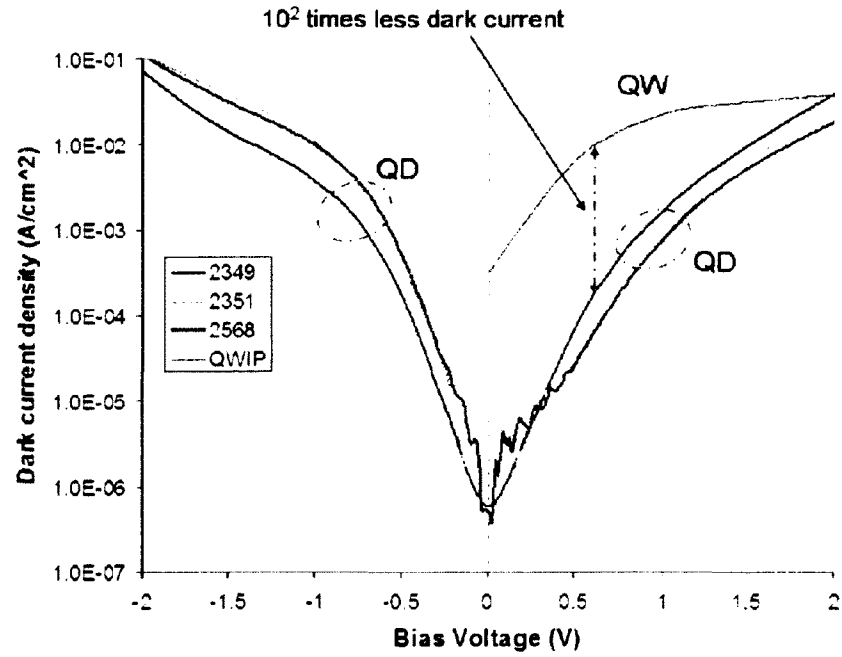
Figure 9, Dark current density of a QDIP as compared with a QWIP. An over 10^2 times less dark current have been demonstrated[17].

(3) High photoconductive gain and responsivity

The 3D confinement carriers and long excited state lifetime [18]—which allows efficient collection of photo-excited carriers and ultimately leads to high photoconductive (PC) gain, high quantum efficiency [19] and photoresponsivity [20] for QDIPs.
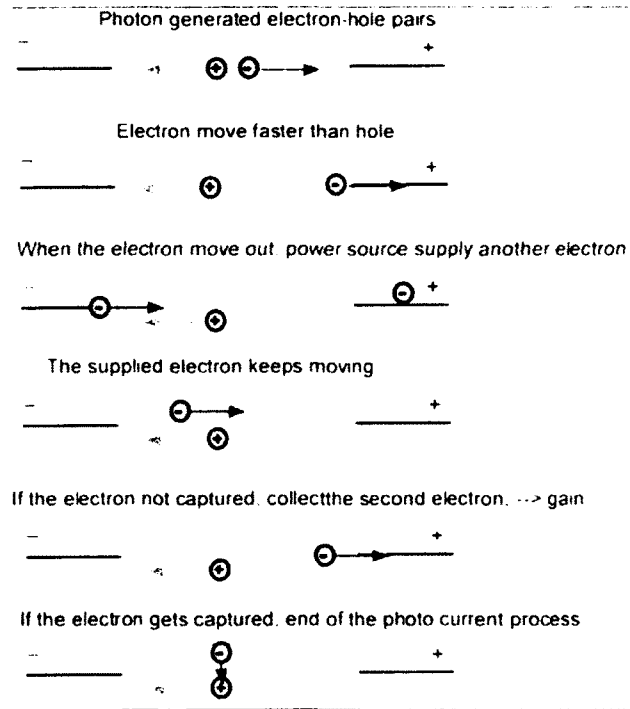
Figure 10, Photoconductive Gain

Figure 10 clearly explains the reason for the high photoconductive gain. Photons coming from the light source will excite the electrons, and thus generate an electron-hole pair. Under the bias, the electron and hole will move in opposite directions, since electron moves faster than hole, and it will finally be collected as photocurrent. After the generated electron being collected, the power source will supply another electron. The supplied electron will keep moving until being captured by the hole, and it will claimed as "Gain" if the electron is collected rather than captured. Generally speaking, the Gain is related to the speed of the hole

movement and the electron capture probability. For quantum dots, once the electron get

excited and leave, the hole can't moving anywhere because of the local confinement, which

will generate more chance to get high photoconductive gain. Also, compared with the

quantum well, the quantum dots have very low capture probability, which means that it can

collect more electrons, and that basically explains why the quantum dots photo detector has

very high photoconductive gain.

In addition, due to the high photoconductive gain (typically 10-100), QDIPs also show

high photoresponsitivities of over 1A/W [18-20]. Such high photoconductive gain and large

photoresponsivity allows QDIPs to detect weak LWIR radiation from a long distance.

(4) High operation temperature

The low dark current together with high photoresponsitivity makes QDIPs promising for

highly sensitive and cryocooler-free operation. Figure11 shows the recent work on high

temperature QDIPs from different groups. We have developed a LWIR QDIP with a high

operation temperature (HOT) of 190K by optimizing the dark current blocking barrier for high

dark current to photocurrent blocking ratio[21] in 2007.   And we also demonstrated a LWIR

QDIP with a high operation temperature (HOT) of over 230K. A high photoresponsivity and

photodetectivity (D*) were obtained.

T (K)

300 K • NWU 2007 [4]   • ANFT/UML 2009 [5] • U Michigan 2005 [2]
       RT D* ~6x10   298 K D* ~10^8 300 K D* ~10^6 cmHz$^{1/2}$/W

260 K   • UFL 2003 [1]
                     260 K 7 6 μm

190 K   • UML 2007 [3]
                              190 K D* ~10^6 cmHz$^{1/2}$/W

       4 2 μm   7 6 μm   9 9 μm   17 μm
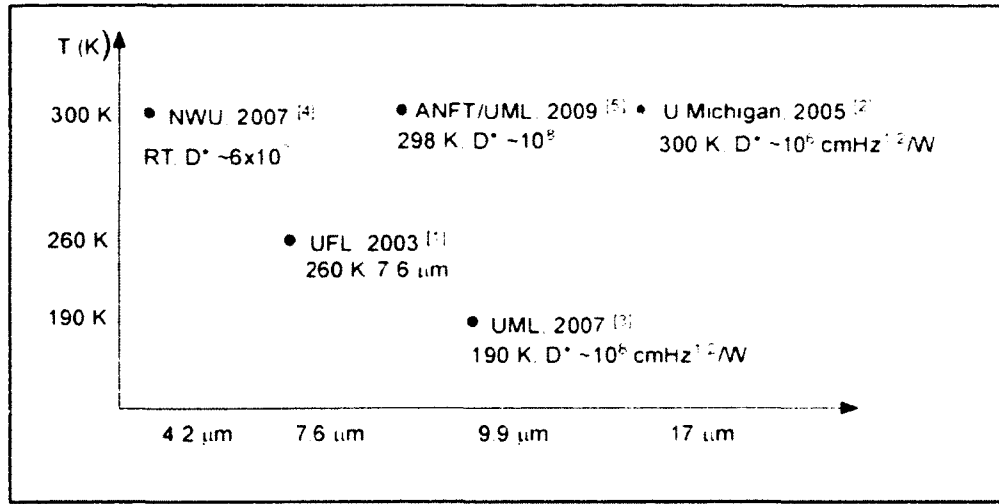
Figure 11, the high operation temperature of QDIPs (1). Appl. Phys. Lett., vol. 82, pp. 1986-1988, 2003[22]; (2) IEEE Photon. Technol. Lett., vol. 16, pp. 1361-1363, 2005[23]; (3) Applied Physics Letters, Vol. 91, pp. 051115, 2007[21]. (4) Appl. Phys. Lett. 90, 131112 (2007)[24]; (5) Proc SPIE vol. 7608-67 (2009)[25].

However, since the total number of QD layers that can be incorporated in a QDIP is limited by the accumulation of strain and the strain induced defects and dislocations, the active QD absorption region is thin. This limits the total percentage of light that can be absorbed in the active region. Accordingly, the QDIP detectivity is still lower than that of the QWIP. This leads to further inconvenience. Therefore, there is need for QDIP to increase its detectivity to match and exceed the performance of current IR detectors. Surface plasmon resonance (SPR), predicted by Ritchie in 1957[26], offers an effective surface light trapping and enhancement technique that enables high efficient light absorption using considerably thinner active light absorption regions [27, 28]. Such SPR surface light trapping and enhancement technique provides a promising solution to overcome the major limitation of the thin active QD region issue in QDIPs. In the next chapter, the details of surface plasmonic resonance and enhancement in infrared sensing will be discussed.

14

CHAPTER II SURFACE PLASMONIC RESONANCE AND ENHANCEMENT IN INFRARED SENSING

2.1 Back ground

Surface plasmonic waves or surface plasmonic polaritons (SPPs), predicted by Ritchie in 1957 [26], are coherent electron oscillation at the surfaces of metal. Figure 12 illustrates the electric-field induced electron density oscillation. The coherent electron oscillations generate electromagnetic waves that can travel along the dielectric/metal interface[26, 29]. SPPs can cover a broad electromagnetic spectrum with the frequency ranging from 0 up to a few hundred tera-Hertz (THz)[30]. Depending on the surface metal structures, certain frequencies of the surface electromagnetic waves can be strongly excited (or absorbed). This is generally referred to as the excitation of SPRs.
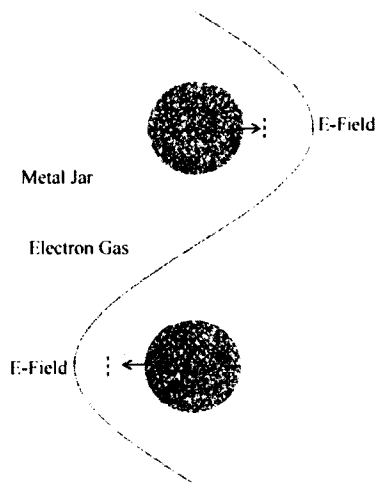
Figure 12, Schematic illustration of the electric-field induced electron density oscillation.[31]

Many structures can excite SPRs, including prism excitation with Otto or Kretschmann configurations[32], metallic nanoparticles, and metallic two-dimensional (2D) subwavelength hole array (2DSHA) [27]. The details of the excitation mechanism are illustrated as below.

2.1.1 Prism Excitation

Figure 13 (a) and 13(b) show two major configurations of SPR excitation using a prism, i.e. Otto and Kretschmann configurations [25], respectively.
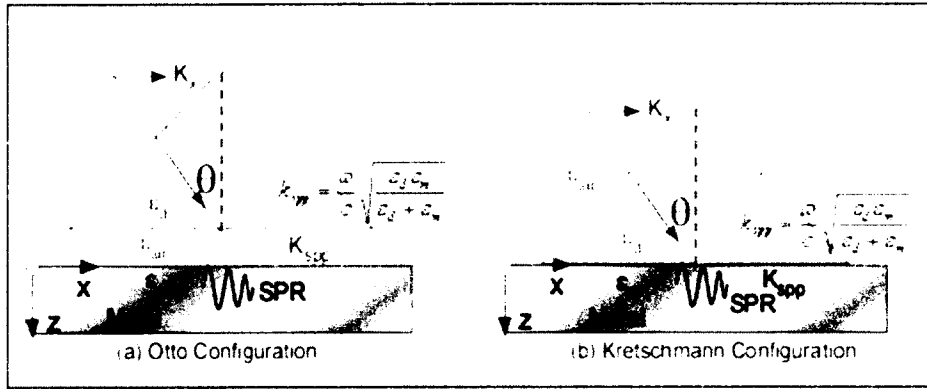
Figure 13, SPR excitation using a prism: (a) Otto configuration; (b) Kretschmann configuration.

The resonant condition for the SPR excitation follows the momentum conservation of the incident light and the SPRs, i.e. the x-component of the wave vector of the incident light $k_x = \frac{\omega}{c}\sqrt{\varepsilon_{air}}\sin\theta$ matches that of the SPP $k_{spp} = \frac{\omega}{c}\sqrt{\frac{\varepsilon_d \varepsilon_m}{\varepsilon_d + \varepsilon_m}}$. The resonant condition can therefore be expressed as:

$$\frac{\omega}{c}\sqrt{\varepsilon_{air}}\sin\theta = \frac{\omega}{c}\sqrt{\frac{\varepsilon_d \varepsilon_m}{\varepsilon_d + \varepsilon_m}}$$

(2.1)

where, ε_{air} , ε_m and ε_d are the permittivities of air, the metal and dielectric at the interface, respectively.

2.1.2 Metallic nanoparticles excitation

In addition to prism excitation, SPRs can also be excited using surface gratings or metal bars (or metal particles), which are shown in Figure 14 (a) and (b), respectively. The resonant condition for the grating-based excitation is

$$\frac{\omega}{c}\sqrt{\varepsilon_{air}}\sin\theta \pm \frac{2\pi}{\Lambda} = \frac{\omega}{c}\sqrt{\frac{\varepsilon_d\varepsilon_m}{\varepsilon_d + \varepsilon_m}}$$

(2.2)

where, Λ is the period of the grating. For the SPR excitation by a metal bar (or metal particles), the reflections at the edges form standing surface plasmonic waves depending on the boundaries. The excitation condition is:

$$\frac{\omega}{c}\sqrt{\varepsilon_{air}}\sin\theta \pm \frac{\pi}{L} = \frac{\omega}{c}\sqrt{\frac{\varepsilon_d\varepsilon_m}{\varepsilon_d + \varepsilon_m}},$$

(2.3)

where, L is the length of the metal bar, or the diameter of the metal particles. Eq. (1) and (3) clear show the strong dependence of the SPR excitation on the permittivities of interface materials the metal ε_m and the dielectrics ε_d .
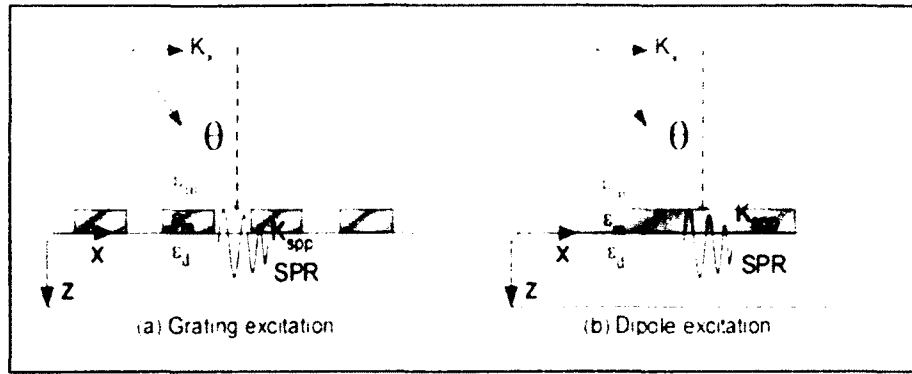
Figure 14, (a) SPR excitation using surface gratings, (b) SPR excitation using a metal bar (dipole excitation).

2.1.3 Metallic 2D hole array excitation

Instead of prism excitation with Otto or Kretschmann configurations [25] and metallic nanoparticles, the metallic two-dimensional (2D) subwavelength hole array (2DSHA) [21] is another promising method to excite the SPRs. Figure 15 (a) shows a picture of a square lattice metallic 2DSHA structure with a 2.6 μm period. Figure 15 (b) shows the simulated E-field profile along the surface normal direction (z direction). It clearly shows the light confinement at the surface.
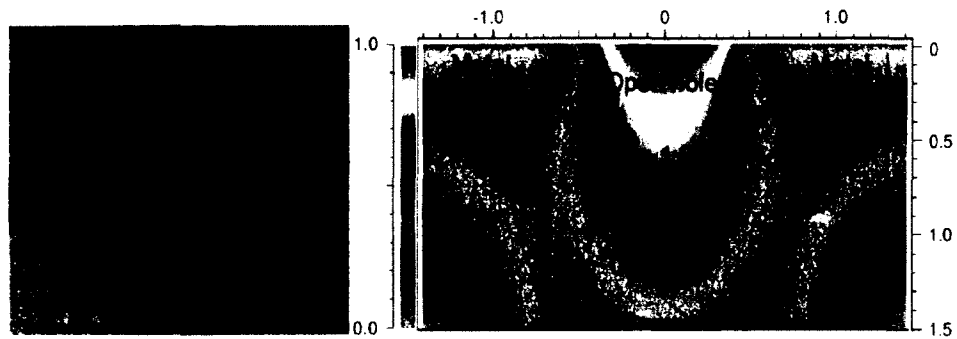
Figure 15, (a) picture of a square lattice metallic 2DSHA structure; (b) Simulated E-field profile.

The resonance wavelength of the plasmonics wave depends on the period of the square

lattice metallic 2DSHA plasmonic structure by [21]:

$$\lambda_{sp} = \frac{d}{\sqrt{i^2 + j^2}} \text{Re}\left\{\left[\frac{\varepsilon_m \varepsilon_d}{\varepsilon_m + \varepsilon_d}\right]^{1/2}\right\},$$

(2.4)

where, d is the lattice constant, (i, j) are the orders of the grating vectors, ε_m and ε_d

are the dielectric constants of the metal and GaAs, respectively. The peak wavelength varies

linearly with the period of the plasmonic structure which is showed below in Figure 16 (a) and

(b).
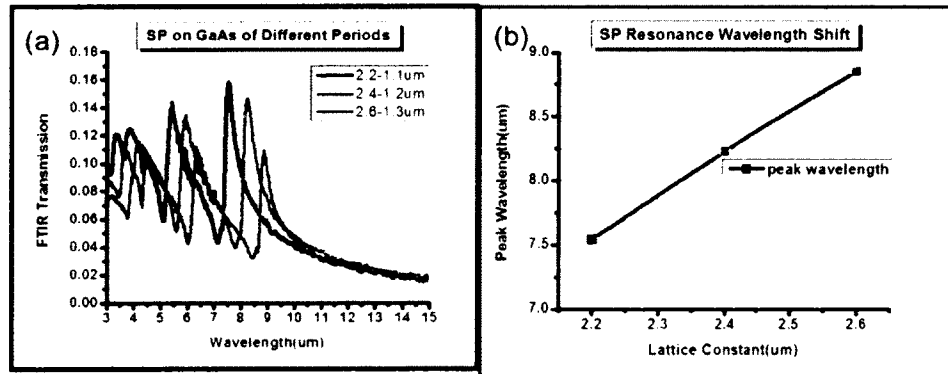
Figure 16, (a) Test results of transmission spectrum for different periods of SP. (b) The peak wavelength varies linearly with the period of the plasmonic structure.[31]

The metallic 2DSHA structure has a few advantages:

(1) Compact and integrated structure. Unlike the prism-based structures, the metallic

2DSHA structure is a very thin layer of metal (typically gold due to its low loss and high

conductivity) with periodical holes. Such a structure can be fabricated on any photodetector

surfaces and form an integrated miniature plasmonic device.

(2) Extraordinary optical transmission (EOT). The metallic 2DSHA structure shows EOT of over 100%. This is primarily due to the light focusing effect in the holes [33, 34]. Figure 15 (b) clearly shows the light focusing at the holes. The EOT property increases the transmission of the plasmonic structure and makes it suitable for filter development.

(3) The surface confinement tunable functionality. The surface confinement can be tuned by varying the 2DSHA parameters[35]. By changing of the hole diameters, the near field spreading in the vertical (surface-normal) direction can be changed.

In conclusion, due to these advantages explained above, the 2DSHA surface plasmonic structure is widely accepted to enhance the photo-response of the infrared quantum dot (QD) photodetectors.

2.2 Previous work for the surface plasmonic enhancement

As seen from the 2DSHA analysis provided above, the parameters of the plasmonic structure will affect the enhancement on the QDIPs, like by changing the period of the 2DSHA structure, one can tune the enhancement peak wavelength. A lot of work has been done in our research group to validate the understanding of the plasmonic theory, and further steps in investigating other parameters of the plasmonic structure like the hole diameters or metal thickness have also been made. Some of the results are illustrated as followed.

2.2.1 Fano-type interference Plasmonic enhancement

A long wave infrared quantum dot photodetector enhanced by Fano-type interference in a

metallic two-dimensional (2D) subwavelength hole array (2DSHA) was reported[36]. The top view and zoom-in view of the QDIP with the metallic 2D subwavelength hole arrays are showed in Figure. 17. The 2D subwavelength hole array is a square lattice with the lattice constant $a = 2.6$ μm. The diameter of the hole is $d = 1.3$ μm. The thickness of the gold film is 50 nm. The photocurrent enhancement wavelength shows an offset from the plasmonic resonant peak and corresponds to a dip in the transmission spectrum of the 2DSHA structure as shown in Figure.18. The offset is attributed to the Fano-type interference in the metallic 2DSHA structure. The asymmetric line shape of the plasmonic resonance is analyzed and it agrees well with the two-peak Fano-type interference model. More than 200% enhancement in photodetectivity and photoresponsivity is achieved at the wavelength of the Fano dip of the first order plasmonic mode. (Figures reprinted with permission from [Vasinajindakaw, P., et al., Appl. Phys. Lett. 98, 211111]. Copyright [2011], AIP Publishing LLC).
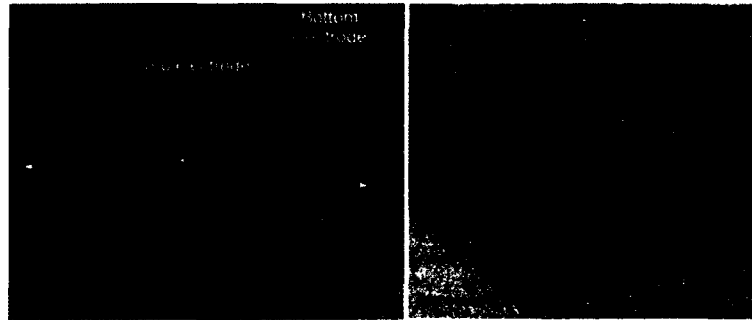
Figure 17, Pictures of the QDIP with the metallic 2D subwavelength hole arrays. (a) top view; (b) zoom-in view.
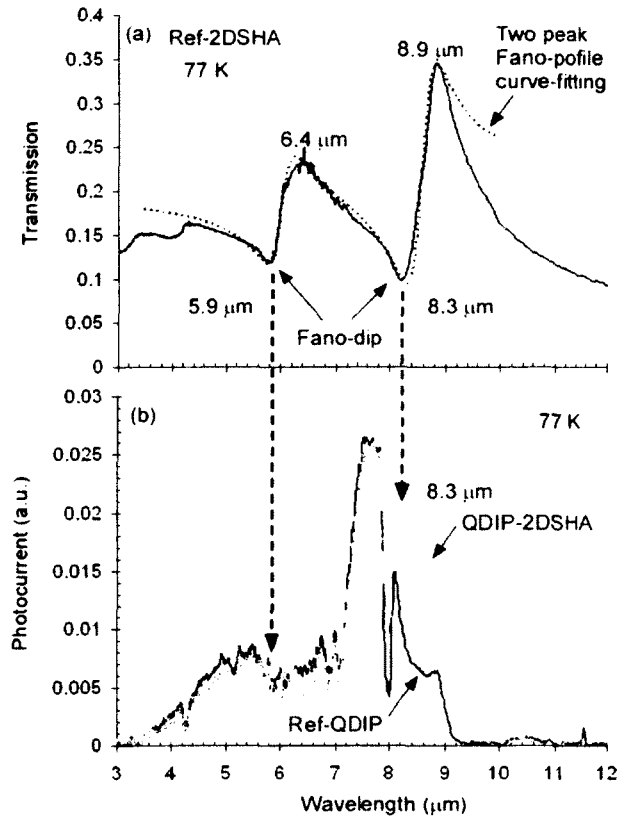
Figure 18, (a) Blue trace: measured FTIR transmission spectrum of the Ref-2DSHA at 77 K, Red dashed line: curve fitting of the two peak Fano-type transmission. (b) FTIR photocurrent spectrum of the QDIP-2DSHA (pink trace) and the Ref-QDIP (blue trace) measured at 77 K.

2.2.2 Polarimetric surface plasmonic enhancement

A surface plasmonic enhanced polarimetric longwave infrared (LWIR) photodetector was reported[37]. The picture of the QDIP with the polarimetric 2DSHA and the zoom-in view of the 2DSHA are shown in Figure. 19. In this study, the 2DSHA is a rectangle lattice with the lattice constants a = 2.6 μm, and b = 3.0 μm in the x- and y- directions, respectively. The diameter of the hole is d = 1.3 μm. The thickness of the gold film is 30 nm. Photo-responses to different polarizations are enhanced at plasmonic resonant modes with different wavelengths as shown in Figure. 20. This allows polarimetric photodetection with band-pass filtering

determined by the plasmonic enhancement profile (Figures reprinted with permission).
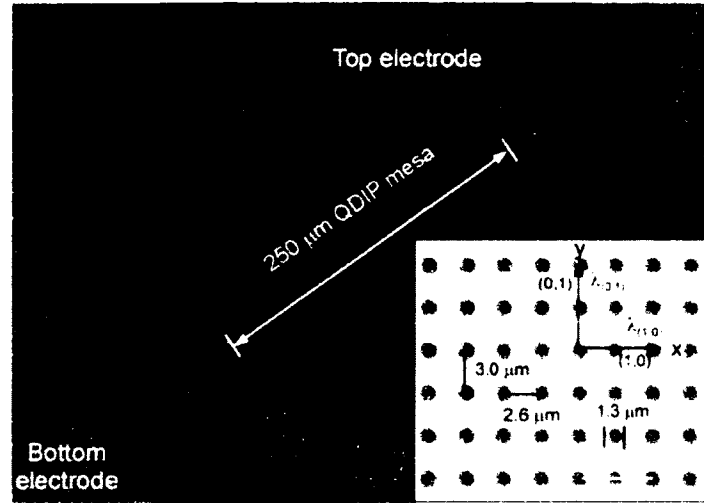
Figure 19, Picture of the QDIP with the 2DSHA. The 2DSHA is a rectangle lattice with the lattice constants a = 2.6 μm, and b = 3.0 μm in the x- and y- directions, respectively.
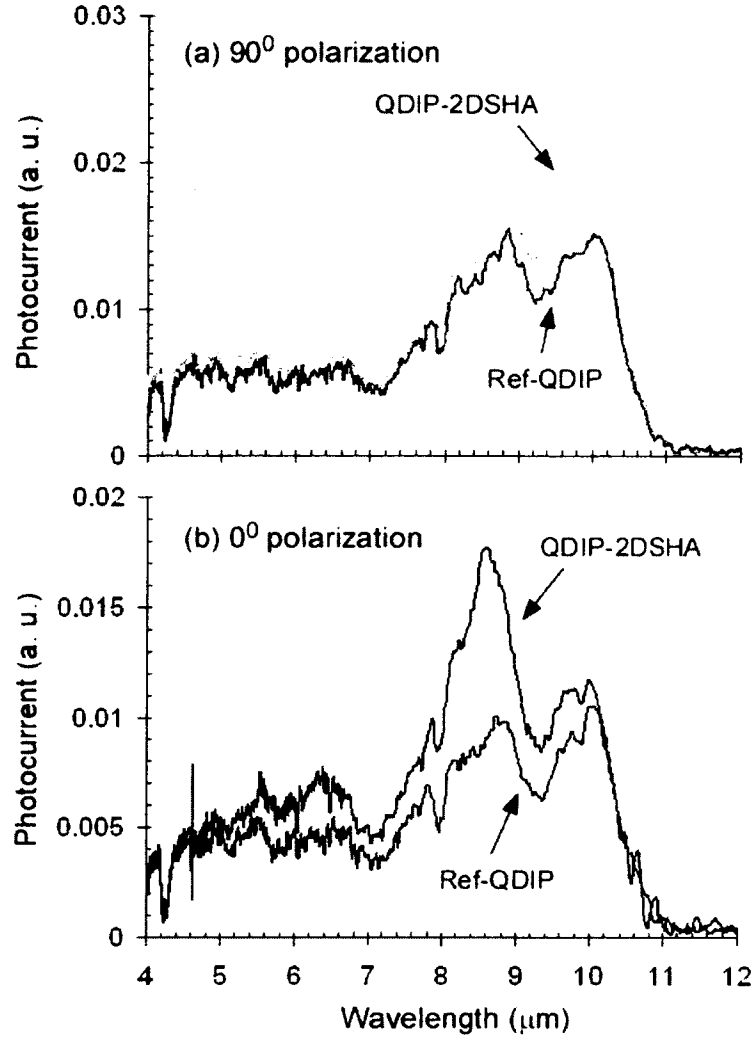
Figure 20, Photocurrent spectra of the QDIP-2DSHA (pink trace for 90 degree polarization, green trace for 0 degree polarization) and the Ref-QDIP (blue trace) at different IR incidence polarizations: (a) 90 degree polarization (y-direction); (b) 0 degree polarization (x-direction).

2.2.3 Surface confinement tuning

In the surface confinement tuning study, we measured the transmission of the 2DSHA surface plasmonic structures and its variation with the hole diameters a of the 2DSHA structures as shown in Figure21. The relationship between the transmission and the hole diameters a is found to be different from the prediction of Bethe's theorem[38]. We also found

24

that the photocurrent of the quantum dot (QD) infrared photodeetctors (QDIPs) with different

active layer thickness show different dependence on the hole diameters a of the 2DSHA

structures. The photocurrent of the QDIPs with 10 active QD layers (10-QDIPs) saturates and

starts to decrease as the hole diameter a is increased more than 1.6 μm, whereas that of the

QDIPs with 20 active QD layers (20-QDIPs) increases linearly with the hole diameter. The

difference in the hole diameter dependence of the 10-QDIPs and the 20-QDIPs is attributed to

the variation of the near field spreading in the vertical (surface-normal) direction due to the

change of the hole diameters. An over 6 time (6x) photocurrent enhancement is obtained by

optimizing the hole diameter of the 2DSHA surface plasmonic structure. The experimental

results are shown in Figure. 22. (Figures reprinted with permission).
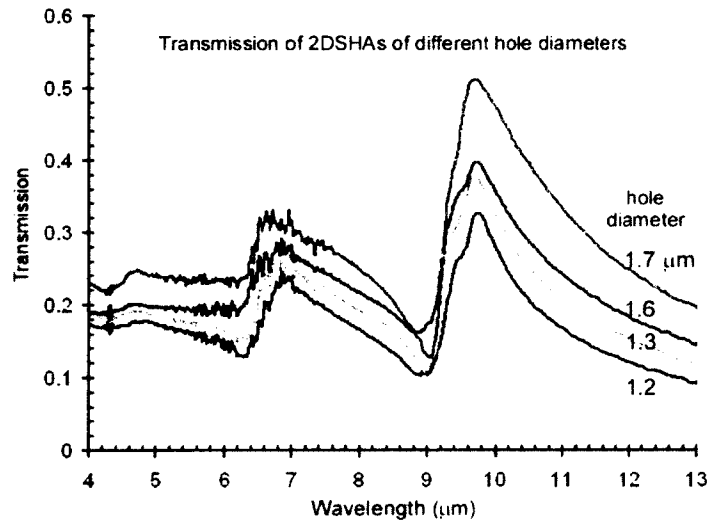
Figure 21, FTIR transmission spectra of the 2DSHA structures of different hole sizes on bare GaAs wafers. The transmission spectral show two group of peaks at 9.7 μm and 6.7 μm wavelength regions, corresponding to the (1,0) (or its degenerate mode (0,1)) and (1,1) orders of the SPWs, respectively.
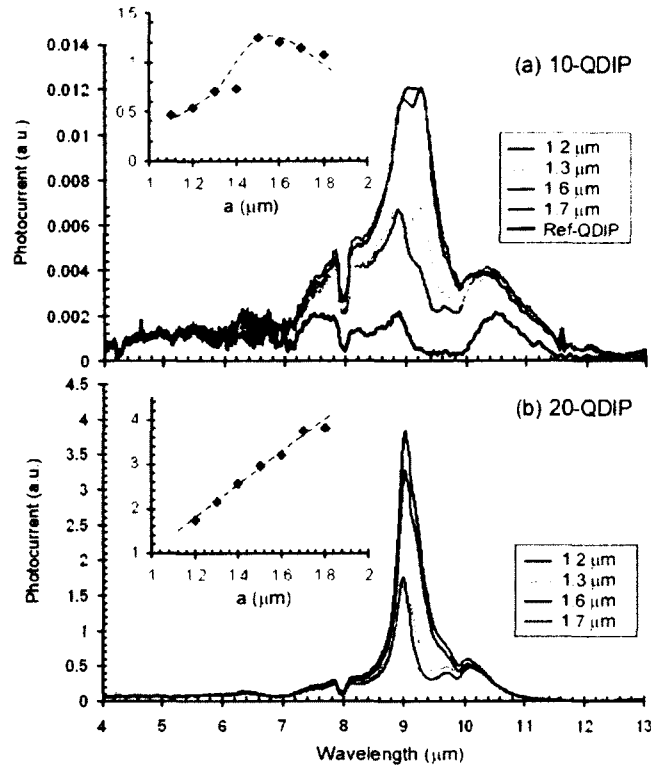
Figure 22, FTIR photocurrent spectra of QDIPs. (a) 10-QDIPs. The inset shows the photocurrent peak values of different hole diameters. The photocurrent is the highest at the hole diameter of a = 1.5 μm and starts to decrease when a is larger than 1.6 μm (b) 20-QDIPs. The inset shows the photocurrent peak values of different hole diameters, the photocurrent increases linearly with the hole diameter a.

CHAPTER III BACKSIDE CONFIGURED PLASMONIC STRUCTURE FOR INFRARED SENSING ENHANCEMENT

3.1 Issues of the top configured plasmonic structure

All the work discussed above can be performed by use of "top-configured" plasmonic to achieve infrared sensing enhancement. whereas "top-configured" refers to the detector equipped with the plasmonic structure on the top surface and the incident light is upon the top

surface as shown in Figure 23. Employing top-configured plasmonic is a common solution to test the device, but not a perfect one. The primary issues of the top configured plasmonic structure are related to its low efficiency, reliability and compatibility.
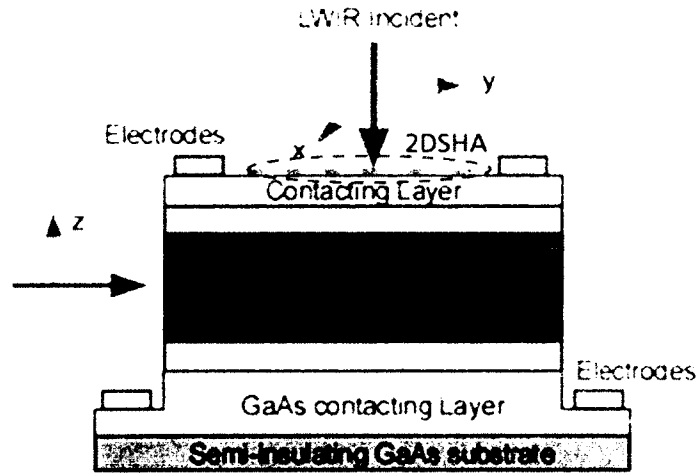
Figure 23. The schematic structure of QDIP with the plasmonic structure on the top surface and the incident light is upon the top surface

(1) Low excitation efficiency

As shown in Figure. 23, the excitation of the plasmonic wave on the metal/semiconductor side is the evanescence waveguide modes through the subwavelength hole array[39]. The intensity of the plasmonic wave on the metal/semiconductor side is therefore dependent on the intensity of the evanescent modes at the output side (i.e. at metal/semiconductor interface). The decay of the evanescence wave is determined by the wave vector component along the z-direction of the evanescent waveguide modes. Nevertheless, for the top-configured plasmonic structure, the excitation of the plasmonic wave at the metal/semiconductor is not efficient due to the evanescent decay of the evanescent modes through the subwavelength

holes.

(2) Poor compatibility with focal plane array fabrication

The focal plane array (FPA) refers to those image sensing devices wherein an array of light-sensing pixels are placed on the focal plane. In fact, each of those pixels is a QDIP. Nevertheless, due to the limitation of the small size of the pixel (~30um), standard wire bonding manipulation does not work for the FPA pixels, while Indium bump is an alternative way to connect the FPA pixels with a read out integration circuit as shown in Figure 24. Apparently, the top-configured plasmonic structure can't be applied to this situation, neither.
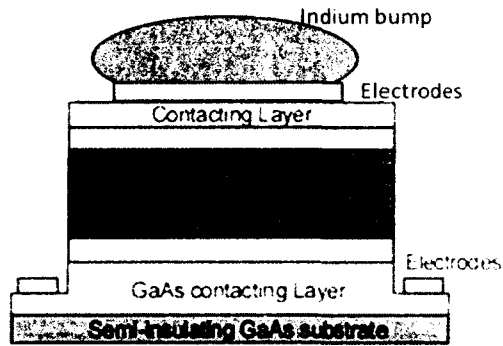
Figure 24, Indium bump for the FPA

Recently, a monolithically integrated plasmonic infrared quantum dot camera had also demonstrated [40]. The surface plasmon structure was integrated on the back side of substrate by interferometric lithography technique. However, fabrication technique is rather complicated and expensive for industrial production. The performance enhancement, as well, has yet to be improved.

(3) Low reliability

The plasmonic structures are made of a 30-nm thin Au film. Since the Au film does not

stick well on GaAs surface, the plasmonic structures are very delicate. They can be scratched away in the fabrication and subsequent packing processes, which makes the plasmonic enhanced FPA unreliable.

To address these issues, in this thesis, I investigate a new backside configured plasmonic structure for the QDIP and FPA enhancement. This type of backside configured plasmonic structure can solve the issues of the low excitation efficiency and provide considerably higher plasmonic enhancement with prominent reliability and excellent compatibility with FPA.

3.2 Backside configured plasmonic enhancement

As used herein, the term "backside configured" refers to a device such that the surface plasmonic structure is configured on the opposite side of the substrate, and the light incident is upon on the substrate side, as showed in Figure 25.
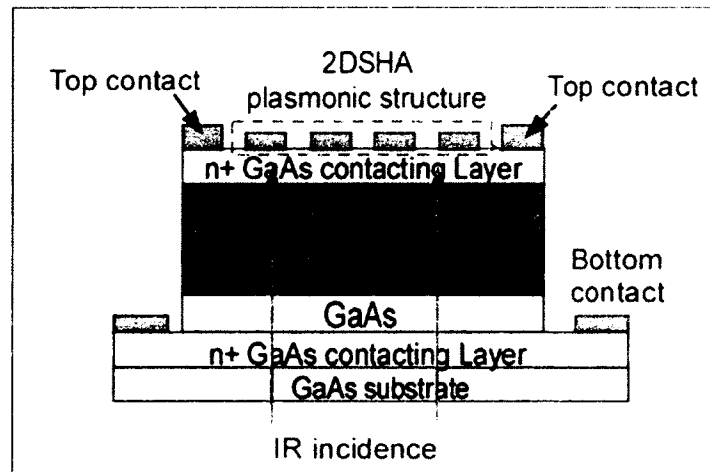
Figure 25, Cross-sectional structure of the backside configured 2DSHA plasmonic structure on the QDIP. The IR incident light illuminates from the substrate side

There are several advantages of the backside configured plasmonic structure:

29

First of all, as for the backside-configured plasmonic structure, the plasmonic resonance is directly excited at the semiconductor/metal surface. The excitation efficiency is much greater than that of the top configured plasmonic structure where the plasmonic wave excitation is excited by the evanescent modes through the subwavelength holes. Due to the higher excitation efficiency, the plasmonic resonance is stronger in the backside-configured plasmonic structure.

Second, all fabrications are carried out on the top side of the sample. Thus, standard photolithography can be used for the fabrication process, which eliminates the complication of fabrication process and reduces fabrication cost together with processing time compared to fabrication of surface plasmon structure on the back side of the sample. Moreover, the distance between the top side surface plasmon structure and quantum dot absorption layer is closer than the back side's one due to the limitation of the polishing process and the standard design of thicker n^+ GaAs contact layer on the bottom electrode. Therefore, the effect of surface plasmon generation is exponentially stronger with a top side surface plasmon structure than a back side surface plasmon structure.

The third advantage comes from the passivation layer. With the top configured plasmonic structure, a SiN_x passivation layer can be easily deposited on top of the plasmonic structure, which will reduce overall dark current and also can protect the thin layer of Au film with high reliability.

The fourth advantage is related to the cross talk of surface plasmon wave on the metal/dielectric interface. The location of each mesa on focal plane array may be very close to

each other, in fact approximately a few microns in distance. A surface plasmon wave from the backside structure generated on one mesa can travel along the metal/dielectric interface and affect the adjacent mesas as long as the metal/dielectric interface is connected. As a result, the cross talk signal is introduced on the back side surface plasmon structure. The smaller distance from one mesa to each other, the stronger cross talk signal interferes with the correct signal. For the backside configured plasmonic structure, the surface plasmon structure on top of each mesa is isolated from all adjacent mesas. So, the cross talk from surface plasmon wave will not be generated. The quality of the picture would be better compared with the backside surface plasmon structure.

With the combination of all four advantages from the designed backside configured plasmonic structure, a higher enhancement on the QDIP infrared sensing with high reliability and excellent compatibility with FPA is expected.

To explore the advantages of backside configured plasmonic structures in infrared sensing, in this thesis, I designed and fabricated the QDIP with 2DSHA plasmonic structure, and conducted tests with the backside configuration. A brief summary of the remaining chapter chapter contents is as follows. The sample growth and device fabrication will be discussed in Chapter 4; Sample characterization and test setup are provided in Chapter5. In Chapter 6, the test results, analysis and discussion will be addressed. Additionally, the advantages of the backside configured plasmonic structure to be further analyzed. Chapter 7 depicts the outline of future research of the thesis work.

CHAPTER IV SAMPLE GROWTH AND DEVICE FABRICATION

4.1 MBE growth

Molecular beam epitaxy (MBE) is one of common methods for epitaxial material growth. Since it can produce high quality films with atomic layer control, the technique is widely used to form quantum wells, quantum dots, tunneling barriers and superlattice. The schematic structure of the main chamber in a typical MBE system is showed in Figure 26 (image from: http://en.wikipedia.org/wiki/Molecular_beam_epitaxy), which include a vacuum chamber, valved sources, and spinning and heated substrate.
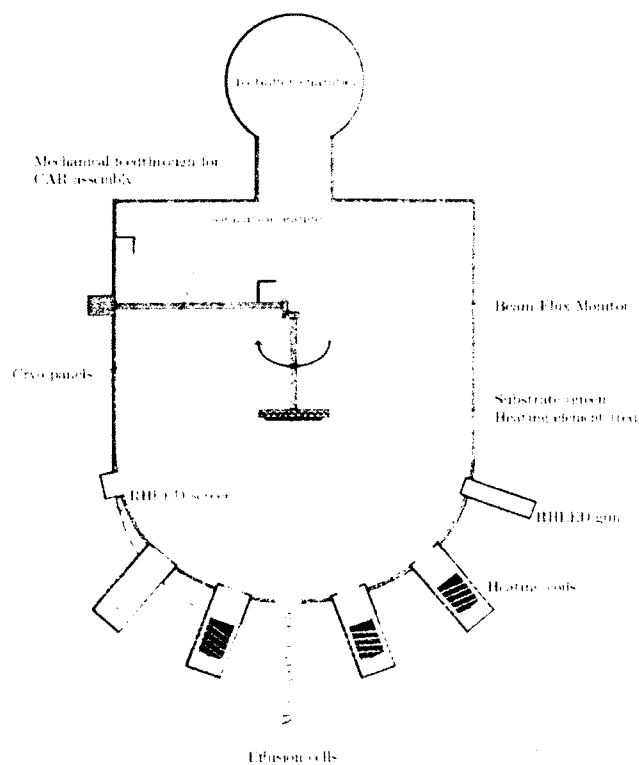
Figure 26, The schematic structure of the main chamber in a Molecular Beam Epitaxy system (image from: http://en.wikipedia.org/wiki/Molecular_beam_epitaxy)

The substrate is mounted on the spinning and heated substrate, placed in the ultra-high vacuum chamber, and deoxidized at high temperature. By opening the valve of the source. material from the effusion cells is grown on the substrate surface. Growth rate is calibrated by a reflective high energy electron diffraction (RHEED) gun. For a regular QDIP, a highly doped contact layer is usually grown on the substrate as the first step. and then followed by a buffer layer, which is used to improve the lattice matching between substrate and quantum dots. Next, various quantum dots layer are grown, followed by a capping layer and finally a contacting layer at the last step. During the MBE process, the size and the shape of the quantum dots can be determined by many factors, such as growth material, growth temperature, growth interruptions, and growth rate.

The QD sample used in the project is UML365, which is grown using a V80H molecular beam expitaxy (MBE) system. A $0.3 \mu m$ Si-doped (n+) GaAs contact layer ($n = 1 \times 10^{18} cm^{-3}$) is first grown on a semi-insulting GaAs (100) wafer, followed by the growth of a 100 nm undoped GaAs buffer layer. The growth temperature for the GaAs contact and buffer layers is 580 °C. The active region of the QDIP consists of ten periods of QD heterostructures. Each period of the QD heterostructures consists of 1 nm $In_{0.15}Ga_{0.85}As$ followed by 2 monolayers (ML) of InAs QDs, 6 nm $In_{0.15}Ga_{0.85}As$ cap layer and 50nm GaAs spacer layer. The doping level of the QD region is tuned to be approximately 5 electrons/dot. The QD layers and the $In_{0.15}Ga_{0.85}As$ cap layers are grown at 485 °C. The top contact layer is a 0.1 μm Si-doped

$(n=1 \times 10^{18} cm^{-3})$ GaAs layer. The cross-section of sample UML365 MBE growth structure and the AFM image of the QDs are showed in Figure 27 and Figure 28, respectively.

UML365 Structure

Surface QDs
GaAs:Si Contact 1000 A
GaAs Buffer 500 A
GaAs Spacer 500 A
InGaAs Cap 60 A
QDs 2ML
QD Well 10 A
Buffer 1000 A
GaAs:Si Contact 3000 A
GaAs Buffer 3000 A
Substrate

x10
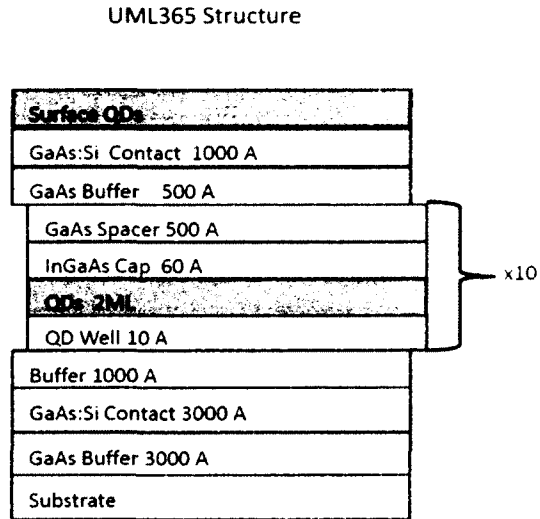
Figure 27, The cross-section of sample UML365 MBE growth structure

(a)   (b)
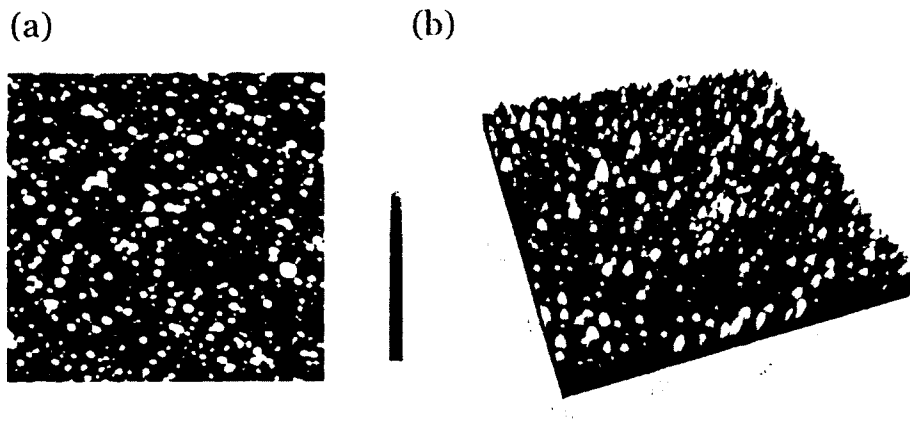
Figure 28, The AFM image of the QD (a) topography (b) 3D view of the QDs

In designing the parameters of the 2DSHA plasmonic structure that can fit the QDIP property, the pick-up wavelength of the detector needs to be predetermined. Then, after the

growth, the wafer is processed into 250 μm-diameter circular QDIPs by regular standard photolithography. The FTIR test result for UML365 is shown in Figure 29.
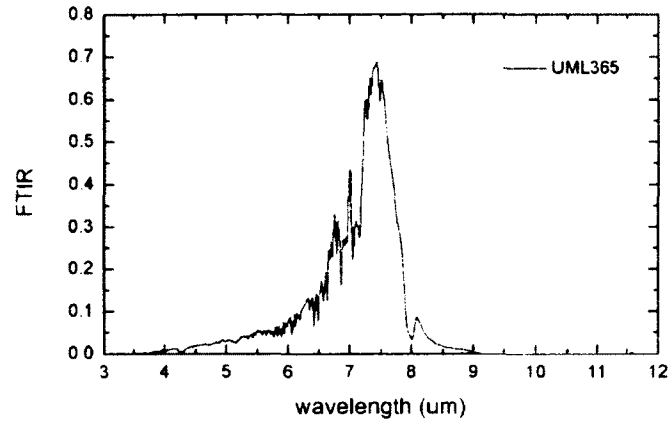
Figure 29, FTIR test result for sample UML365

As seen from the test result, the pickup wavelength ranges from 4 μm to 9 μm with the peak around 7.5 μm. According to the 2DSHA plasmonic theory discussed earlier in section 2.1.3 of Chapter 2, the plasmonic lattice constant is designed to be 2.3 μm and the hole size is set for 1.15 μm. However, the hole size is too small to be fabricated using the standard photolithography. Alternatively, such small size fabrication can be achieved using the E-beam lithography. Due to the alignment issue, the plasmonic structure was first fabricated on the top of the wafer, then the standard QDIPs are aligned with the SP structure, after that it tales standard photolithography process and finally E-beam metal deposition process.

4.2 Device Fabrication

4.2.1 E-beam lithography for the SP pattern

As a higher resolution alternative to photolithography, Electron Beam (E-beam) Lithography emits a beam of accelerated electrons across a surface covered with a charge-sensitive resist layer and then removes selected regions from the resist.

The primary advantage of E-beam lithography is that it is one of the effective ways to enable the precise exposure controls in a few nanometer regime and create very small structures with high-quality geometrical control. Furthermore, its relatively low energies allow for high resolution and at the meanwhile avoid a considerable amount of backscattering and substrate damage.

However, the main limitation of E-beam lithography is the long exposure time it takes. Besides this, high-resolution resists often requires its thickness less than 100 nm, which makes exposure more rigorous and users not be able to use the mask for thicker metal lift off.

In this work, the PMMA950 2A is used as the electron beam resist. Before spin coat with PMMA, the sample needs to be deoxidized and dehydrated in Oxygen plasma. During writing, the beam energy is 100keV, and probe current is 1nA. After dose test, the exposure dose was fixed at 0.15s for the 2DSHA structure. It takes about 10min for a 100umX100um area.

After exposure, the pattern is developed in MIBK: IPA=1:3 solvent for 1min and then rinsed with IPA. After developing, the sample was then processed with 25nm Au deposition and lift off. The microscope image of the 2DSHA structure is shown in Figure 30.
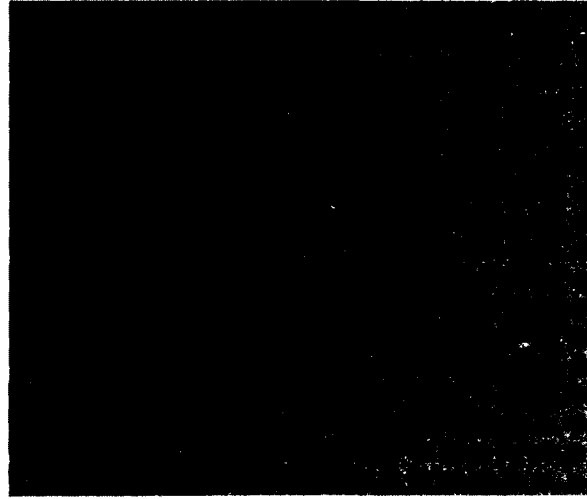
Figure 30, Microscope image of the 2DSHA by E-beam lithography

4.2.2 Fabrication processes for QDIPs

Standard photo-lithography and wet etching were performed on the wafer with 2DSHA surface plasmonic structure to form individual QDIPs. The top and electrodes were formed by standard E-beam metal deposition and lift-off metalization procedures followed by rapid thermal annealing (RTA) to ensure Ohmic contacts were produced on both of the top and bottom electrodes. The fabrication processes of QDIPs are schematically demonstrated in Figure 31(a) through Figure 31(j):
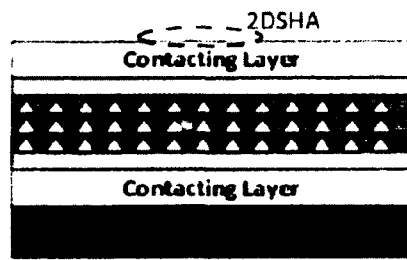
31(a) Wafer with SP
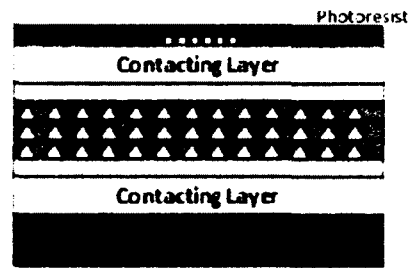
31(b) Spin coat with photoresist
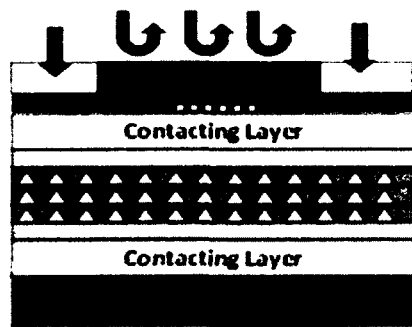
31(c) UV exposure with mask
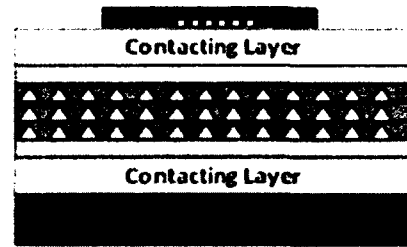
31(d) Develop with CD30
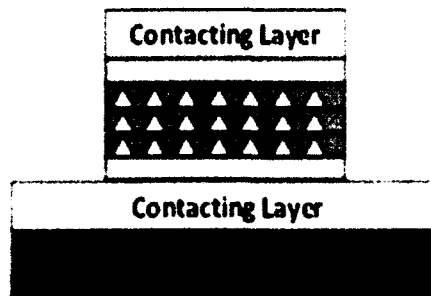
31(e) Wet etch
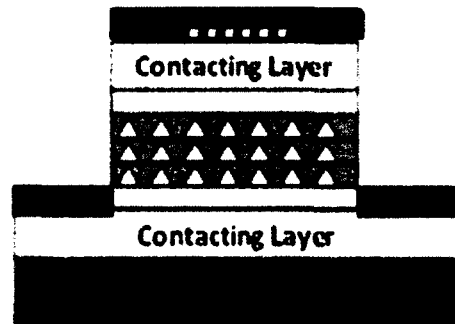
31(f) Spin coat with photoresist

38
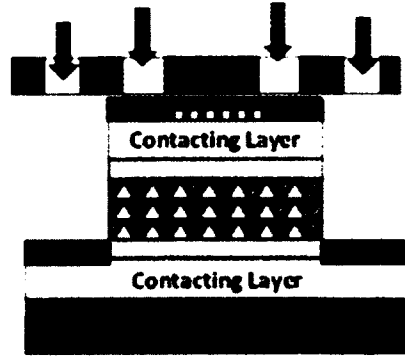
31(g) UV exposure with electrode mask   31(h) Develop with CD 30
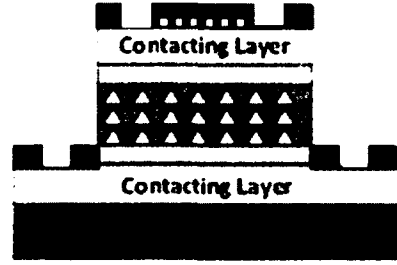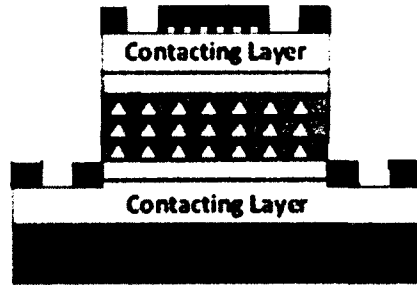
31(i) E-beam metal deposition   31 (j) Lift off
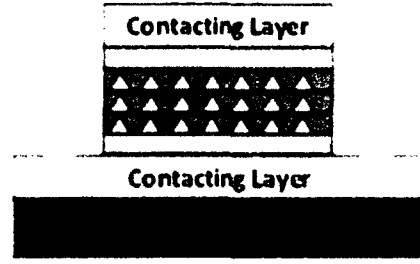
Figure 31, (a)-(j) the fabrication processes of QDIPs

Figure 31(a) depicts the wafer with 2DSHA structure on its top surface. Then it was

followed by the standard QDIP fabrication processed in Harvard cleanroom. First of all, the

wafer should be cleaned very gently; then, a layer of positive photoresist (S1822) was

spin-coated on the top surface as shown in 31(b). Next, the sample was soft baked at 100 °C

for 2min. In order to obtain the desired patterns, the wafer was covered by a photomask which

is aligned with the 2DSHA pattern and then exposed with UV light, as illustrated in Figure

31(c). The photomask can allow the light to pass through the open channel and block out the

light that hit on the dark area, because positive photoresists become soluble after being

exposed in UV light. Once the sample was dipped into the CD-30 developer for 1min, the area

protected by mask remained the same, but the part under exposure was washed away.

therefore. the patterns had been transferred from the mask to the wafer as shown in Figure

31(d). In the next step, the wafer was then etched by using piranha etch solution containing

sulfuric acid (H_2SO_4): hydrogen peroxide (H_2O_2): water (H_2O) in the ratio of 1: 8: 80 by

volume, then the QDIPs mesas as shown in Figure 31(e) were formed during this wet etching

process. As seen in Figure 31(f), the wafer was then spin-coated and soft baked again as

before. Afterwards, we applied the electrode photomask, aligned it with the mesa array, and

exposed once again, then the metal electrode pattern was imprinted on the wafer like Figure

31(h). Finally, the standard E-beam metal deposition 31(i) and lift-off 31(j) procedures were

applied on the sample. As described in the figures, the top and bottom electrodes are formed at

the same time, each of which are composed of a combination of Ni:Ge:Au:Ni:Au layers with

layer thickness of 50Å, 170 Å, 330Å, 150Å, and 3000Å, respectively. After that, the metal

layers are annealed by rapid thermal annealing (RTA) at 460°C for 5s, in which ohmic

contacts between the electrodes and the contact layers have been achieved. The microscope

images of the finished sample were provided in Figure 32. Figure 32(a) is the refer QDIP

without SP structure on and (b) aligned with 2DSHA structure on the top of the mesa. (c) is

the zoom in figure of the mesa with the SP structure and (d) is the zoom in image of the
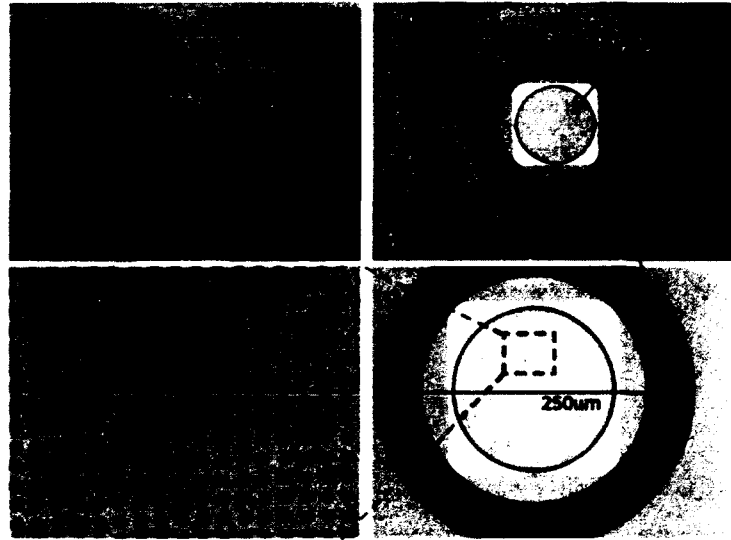
2DSHA.

Figure 32, The microscope images of the finished sample. (a) is the refer QDIP without SP structure; (b) aligned with 2DSHA structure on the top of the mesa. (c) is the zoom in figure of the mesa with the SP structure and (d) is the zoom in image of the 2DSHA.

As so far, the QDIP with 2DSHA surface plasmonic structure was fabricated. Further preparation steps need to be performed before performing the test. Next to the cleanroom fabrication on the sample, the backside of the substrate was polished in order to accomplish the backside configuration. Then the sample was mounted on a copper plate, in which a small hole was drilled to allow the light to pass through the backside of the sample as shown in Figure 33. The sample needs to be carefully aligned with the hole, in order to allow light illuminates exactly on the detector.

Copper plate with a hole

Backside
polished QDIPs
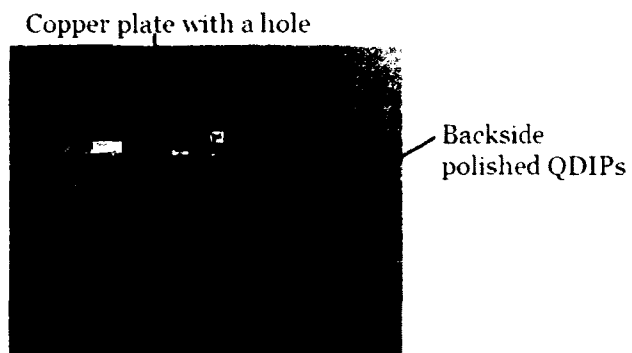
Figure 33, Copper plate with a hole. The sample substrate was polished

Next, the top and bottom electrodes were connected to the standard PCB board by wire bonding in preparation of further tests, where the view of the mounted QDIP sample was displayed in Figure 34[41]. Now, the sample is ready to be tested for all the detector performance parameters.

PCB board   Wire bonding
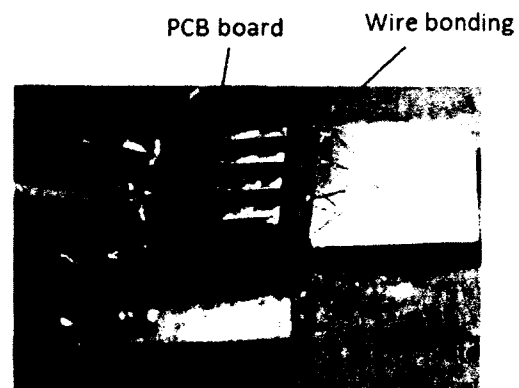
Figure 34, Photograph of the mounted QDIP sample[41]

CHAPTER V QDIP CHARACTERIZATION AND TEST SETUP

5.1 Overview of the characterization

For the QDIP characterization, we look at several detector performance parameters such as detection spectrum, photocurrent, noise current, dark current, noise (signal to noise ratio), photoconductive gain, responsivity (voltage or current per unit of input power), detectivity (sensitivity of detector with respect to area and frequency bandwidth), and quantum efficiency. These parameters will be either measured or calculated and then used as figures of merit for the photodetector performance.

The overview of characterization setup in our lab is shown in Figure 35. The sample is placed in the chamber filled with liquid nitrogen to keep the sample at low temperature. Next to the chamber is the FTIR spectrometer, which is used to test the spectral response of the QDIP. On the right side of the FTIR sits the blackbody source used as the light source during the photocurrent test. And in front of the blackbody source, there is a chopper which can modulate the blackbody source at a constant angular frequency. Temperature controller, preamplifier and spectrum analyzer are on the right top of the shelf. The temperature controller is connected to the chamber and controls the sample's temperature during all the test processes. The preamplifier adds bias on the sample during the FTIR, photocurrent and noise current test. And the spectrum analyzer collects the photocurrent and noise current information. At last, the source meter, which is used for the dark current test, is on the right bottom corner.
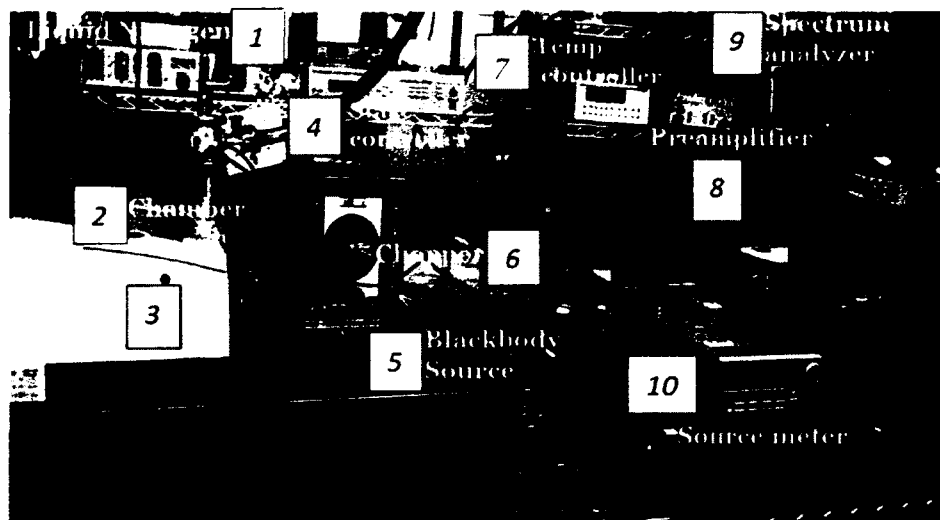
Figure 35 Photograph of the QDIP characterization setup: (1) Liquid Nitrogen Transfer hose; (2) Chamber; (3)FTIR; (4) Stage controller; (5) Blackbody Source; (6) Chopper; (7)Temperature Controller; (8) Preamplifier; (9) FFT Spectrum Analyzer; (10) Source meter

Before going to the actual test, it will be beneficial to outline the parameters in evaluating the QDIP performance. The detailed information of the performance parameters, test setup for the measurements and the parameter calculations are illustrated as follows.

5.2 Measured Parameters and setups

5.2.1 Detection spectrum (FTIR)

The spectral response of the QDIP is typically measured by a Fourier transform infrared (FTIR) spectrometer. Figure 36 shows the schematic structure and principle of a FTIR spectrometer. As presented in the figure, the main parts of the FTIR include fixed and moveable mirrors, beam splitter, IR source and detector. The beam splitter can separate the beam from the IR source into two paths, beam 1 and beam 2. These two beams are reflected by the moveable

mirror and fixed mirror respectively, and then recombine at the beam splitter and pass through

the sample. Because of the continually changing position of the moveable mirror, the lengths of

optical path between the two beams are always different, which will result in interferogram.

Every data point (a function of the moving mirror position) of the interferogram contained the

information about every infrared frequency (wavenumber). By performing the Fourier

Transformation, the wavelength information of the sample can thus be obtained from the

position.
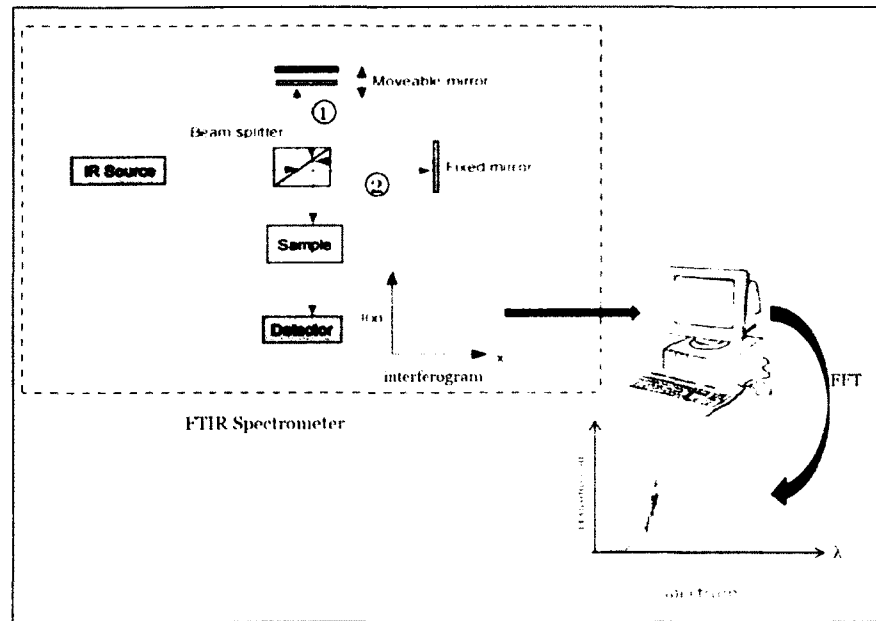
Figure 36 Principle of the Fourier transform infrared (FTIR) spectrometer.

The interference of the two reflected beams can be written as [17]:

$$I(x) = |E_1 + E_2|^2 = E_1^2 + E_2^2 + 2E_1E_2 \cos(\theta) = \frac{I_0}{2}\left[1 + \cos\left(\frac{2\pi}{\lambda}x\right)\right],$$ (5.1)

where, I_0 is the intensity of the incident IR beam, λ is the wavelength and x is the position. Since the IR source contains many different frequencies (wavelengthes), the interferogram can be expressed as:

$$I(x) = \int_0^\infty \frac{I_0}{2}\left[1 + \cos(2\pi v x)\right]G(v)dv ,$$

(5.2)

where, $G(v)$ is the transmission profile of the sample;

v is the wave number.

$$I(x) = \int_0^\infty \frac{I_0}{2}G(v)dv + \int_0^\infty \frac{I_0}{2}\cos(2\pi v x)G(v)dv$$
$$= \frac{I_0}{2} + \int_0^\infty \frac{I_0}{2}\cos(2\pi v x)G(v)dv$$

(5.3)

The AC part of I(x), is actually Fourier transform of the transmission profile of the sample, $G(v)$, which be obtained by performing a reverse Fourier transform.

$$G(v) = \int_{-x}^{x} I(x)\exp(-j(2\pi v x)dx ,$$

(5.4)

In practical situation, the position x can not move from $-\infty$ to ∞. The resolution of the FTIR system is determined by the maximum movement x_{max}:

$$\text{Resolution} \propto \frac{1}{2\pi x_{max}} ,$$

(5.5)

The QDIP detection spectrum in our lab was measured by a Bruker Optics Tensor27 FTIR spectrometer. The schematic lab test setup for the spectral response measurements is shown in Figure 37. In the spectral response test, the QDIP sample which was mounted on the copper plate as shown in Figure 34 was secured on a cooling finger in the characterization chamber

46

(Janis, model No: ST-100) and connected to the preamplifier (Stanford research systems, model SR570) in order to apply bias on the sample. The chamber was placed into the FTIR body and aligned with the IR source as shown in Figure 37. During the test, the cooling finger mounted with sample is filled with liquid nitrogen and the temperature is controlled by the temperature controller (Lakeshore, 331 Temperature Controller).
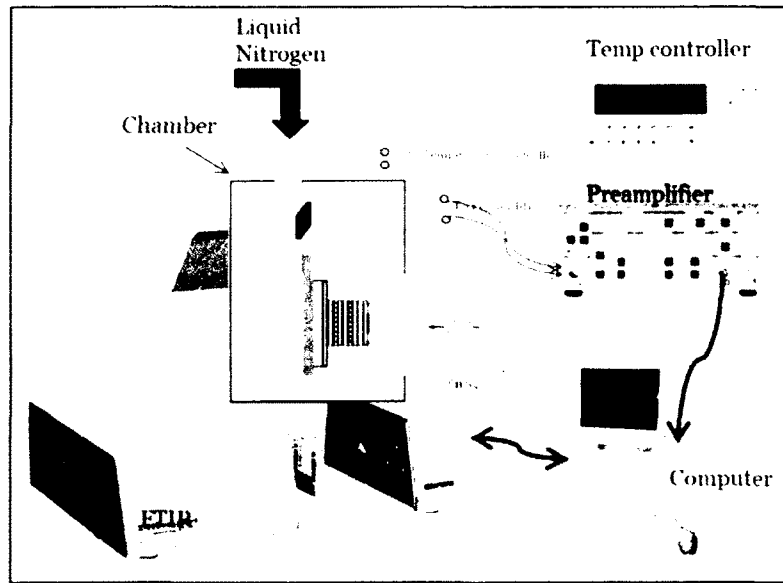
Figure 37 Schematic FTIR test setup for the QDIP detection spectrum.

Figure 37 illustrates a standard QDIP FTIR test for the top configured illumination, as shown in the figure where the infrared light is shining on the top surface of the QDIP sample. However, for the backside configuration of FTIR test, the sample was placed on the other side of the finger in the chamber as shown in Figure 38. In order to allow the light source to illuminate on the substrate of the QDIP sample, a hole was drilled in the copper plate as shown in Figure 33 and the QDIP detectors are aligned with the hole. To compare the performance of

the top and backside configured plasmonic structures. both the top and back illuminations are

essentials. And after one of the tests is completed at low temperature, the sample needs to be

warmed up to room temperature and changed the position, then moved on for the next test.
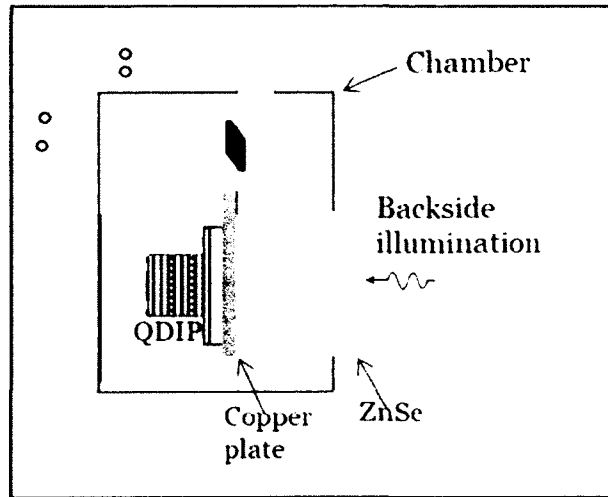
Figure 38 Schematic graph of backside configuration of the QDIP

5.2.2 Photocurrent

As illustrated in Chapter 1, part 1.2.2 Photodetecter-Quantum Dots detector, the electrons

at the lower energy level are excited by the IR light source and subsequently collected through

the top electrode and generate photocurrent. So photocurrent is an essential parameter to

characterize the detector. The experiment setup for the photocurrent test is shown in Figure 39.
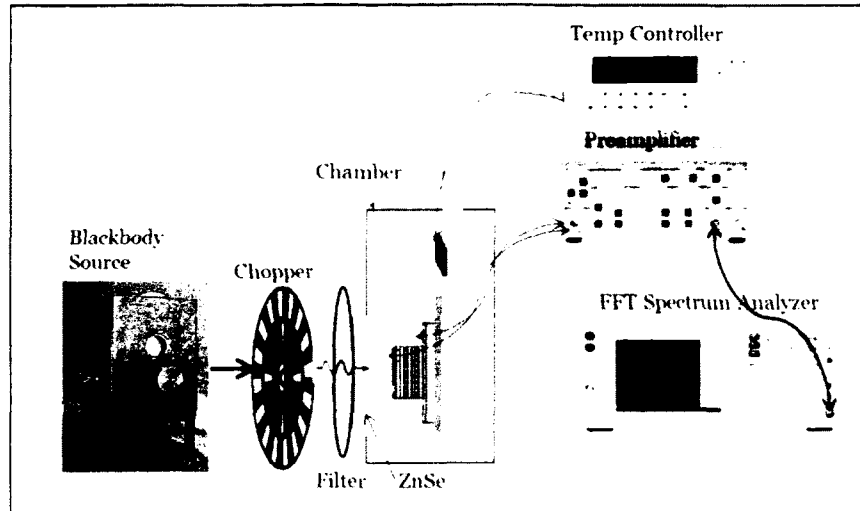
Figure 39 Schematic graph of photocurrent test setup in our lab

The blackbody used in this setup is an SBIR microprocessor controlled cavity blackbody.

The infrared source is normally modulated at a constant angular frequency by using a rotating

multi-bladed wheel (chopper) between the radiation source and the photodetector. The spectral

responsivity was calibrated with the blackbody source at the temperature of 1000 ($\pm$0.1) K and a

modulation frequency of 600 ($\pm$0.3) Hz.

In the photocurrent test, the black body (SBIR, Santa Barbara Infrared INC) emits

infrared light which will pass through an outside chopper shown in Figure 39 at frequency 600

Hz. Next, the modulated light passes through an optical filter (depending on wavelength

selection) which will filter the spectrum into the desired infrared band. Then the filtered light

reaches the device in the chamber through ZnSe window (3-14µm, Transmittance = 60%). The

sample was mounted on the finger in the chamber, and cooled down with liquid nitrogen the

same as FTIR test. For the backside configuration, the sample's position needs to be changed

as illustrated in Figure 38. By being exposed with the blackbody IR light, the photocurrent

49

generated in the QDIP sample flows due to electrical field provided by the preamplifier. The photocurrent is then collected by the spectrum analyzer (Standford research systems, model SR760 FFT spectrum analyzer), which reads the photocurrent at 600Hz in order to reduce the 1/f noise.

5.2.3 Noise current

Noise refers to random fluctuations in photo-voltage or photo-current coming from several different sources. There are mainly four noise sources in photodetectors: Johnson noise, 1/f noise, generation-recombination (G-R) noise, and preamplifier noise. Usually, at low frequencies, 1/f noise is dominant, so during the test we use 600Hz frequency to avoid the 1/f noise. The preamplifier used in the test is carefully determined with very low noise, thus the preamplifier noise is negligible. Therefore, the major noise sources for the noise current are Johnson noise and G-R noise.

The noise current was measured using a Stanford Research SR760, FFT Spectrum Analyzer in our lab. The schematic graph of the measurement setup is shown in Figure 40. Similar as the photocurrent test, the temperature controller controls the sample temperature, while the bias is applied on the QDIP sample by the preamplifier, and spectrum analyzer is used to store the noise data. Distinction from the photo current test is that the blackbody light source was removed, and the chamber was covered by aluminum foil to block any possible light source. In this way, the noise which includes G-R and Johnson noise is recorded.
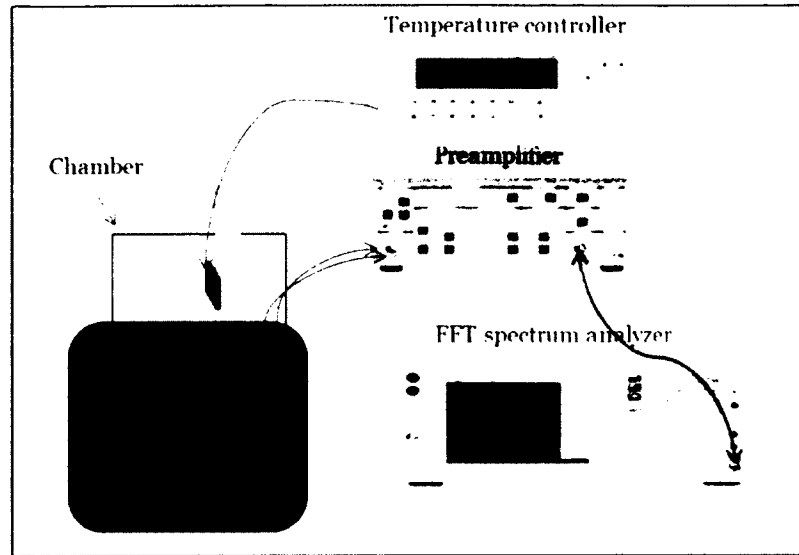
Figure 40 Schematic graph of noise current measurement setup

5.2.4 Dark current

Dark current can be measured through a source meter. For the dark current test set up as shown in Figure 41, the chamber is covered with aluminum foil so that no light can reach and expose the photodetector. The dark current (I_{dark}) is measured using Keithley 2602 System Source meter with the LabTracer program in our lab. The source meter applied a sweep bias on the QDIP and simultaneously collects the relative current at each bias. Then I-V characteristics are generated by this procedure.
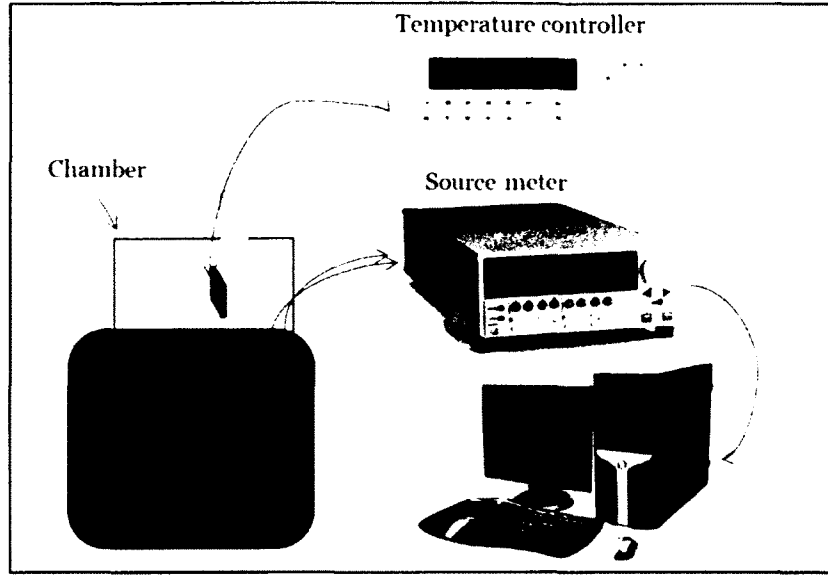
Figure 41 Schematic structure of dark current test setup

5.3 Calculated Parameters

5.3.1 Noise and Photoconductive Gain

As mentioned in last section, the noise current i_{noise} contains generation-recombination (G-R) noise current and thermal noise (Johnson noise) current I_{th} , since the 1/f noise was avoided by applying test at high frequency (~600Hz), and the preamplifier noise is negligible, the noise current can be illustrate as[17]:

$$i_{noise}^2 = 4eG_n I_d + I_{th}^2,$$ (5.6)

where, i_{noise} is the noise current measured in section 5.2.3;

G_n is the noise gain;

e is the charge of an electron (1.6×10^{-19}C);

I_d is the dark current of the QDIP, which is measured using the source meter in the

section 5.2.4.

The thermal noise current can be calculated using:

$$I_{th} = \sqrt{\frac{4kT}{R}},$$ (5.7)

where, k is Boltzmann's constant;

T is the absolute temperature;

R is the differential resistance of the QDIP, which can be extracted from the slope of

the dark current.

The noise gain G_n can thus be calculated from Eq. (5.6) and Eq. (5.7):

$$G_n = \frac{i_{noise}^2 - 4kT/R}{4eI_d},$$ (5.8)

As a good approximation, the photoconductive (PC) gain G equals the noise gain for

conventional QDIP. The photoconductive gain can thus be calculated.

5.3.2 Photoresponsivity

The photoresponsivity ℜ characterizes the performance of photodetector in term of

photocurrent generated per incident optical power at specific wavelength range. The unit for

responsivity is A/W. The total number of incident photons on the QDIPs can be determined by

calculating the blackbody emission at the detector's peak wavelength with passband. The

photoresponsivity of the QDIP can be calculated by:

$$\Re = \frac{4\pi I_{ph}}{P_d \Delta\Omega \Delta v},$$ (5.9)

where, I_{ph} is the photocurrent of the detector;

P_d is the power spectral density of the cavity blackbody at 1000K; $\Delta\Omega$ is the solid angle of the photodetector, and Δv is the spectral width of the detector.

The solid angle of the photodetector can be written as:

$$\Delta\Omega = \frac{\pi D^2}{R^2},$$ (5.10)

where, D is the diameter of the photodetector;

R is the distance from the blackbody to the photodettector.

As seen from the equations above, the incident optical power depends on the opening area of the photodetector surface, solid angle in the test set up, photodetector pick-up wavelength and also the transmittance of optical filter, ZnSe window and photodetector itself.

5.3.3 Photodetectivity

Photodetectivity determines the capability of a photodetector to detect the weak signals. It is the sensitivity of the detector which normalized to 1 cm^2 area and 1 Hz of noise-equivalent bandwidth, The unit for detectivity is $cm \cdot H_z^{1\,2}/W$. A larger detectivity means a higher signal to noise ratio (SNR).

The photodetectivity D* can be expressed as:

$$D^{\cdot} = \frac{\Re\sqrt{A}}{i_{noise}},$$

(5.11)

Where, A is an opening area that the photodetector exposes to the IR radiation;

$\Re$ is photoresponsivity;

i_{noise} is the measured noise current.

5.3.4 Quantum efficiency

The quantum efficiency (QE) is incident photons to converted electrons ratio. It is an important parameter to characterize the QDIPs, since it measures a device's electrical sensitivity to light. By the definition, the quantum efficiency can be calculated:

$$QE = \frac{Electrons / s}{Photons / s} = \frac{I_{Ph} / eG}{P_0 / (hc / \lambda)} = \frac{\Re}{\lambda} \cdot \frac{hc}{eG},$$

(5.12)

Where, $\Re$ is the responsivity from Eq. 5.9;

λ is the wavelength;

h is the Planck's constant;

c is the speed of light;

e is the electron charge;

G is the photoconductive Gain, calculated from Eq. 5.8

So for, all of the QDIP performance parameters and characterization setups have been introduced. In the following chapter, test results, analysis and discussion of the backside configured plasmonic structure will be discussed. In chapter VI, three different projects will be presented to provide a deep view of the study. Each of the projects will be initiated from simple introduction, followed by test results, and the analysis with simulations or discussions.

CHAPTER VI TEST RESULTS AND DISCUSSION

From the previous chapters' introductions, we have established an overview of the purpose of the backside configured plasmonic structure study (chapter III), the sample growth and fabrication (chapter IV) and the sample characterization (chapter V). In this chapter, three different projects related to the backside configured plasmonic structure enhancement with detailed test results will be presented and discussed.

6.1 Backside configured surface plasmonic enhancement

6.1.1 Introduction

QDIPs enhanced by metallic two-dimensional (2D) subwavelength hole array (2DSHA) plasmonic structures have been reported [34, 36, 42]. In most of these QDIPs, the metallic 2DSHA plasmonic structures are fabricated on the top of the QDIPs. The QDIPs are illuminated from the 2DSHA plasmonic structure side and get enhanced through the extraordinary optical transmission (EOT) effect of the metallic 2DSHA plasmonic structures

[27]. We refer this configuration as the top-configured plasmonic structure, henceforth. QDIPs are also reported to be illuminated from the QDIP side (back illumination) [43]. Light illumination direction-dependent plasmonic is observed with the back illumination showing higher enhancement [43]. The higher plasmonic enhancement is attributed to the more efficient SPR excitation. However, the physical mechanism of the more efficient SPR excitation is still not clear.

In this project, over 40 times peak photocurrent enhancement in a backside-configured 2DSHA plasmonic structure enhanced QDIP will be reported. In this configuration, the 2DSHA plasmonic structures are still fabricated on top of a QDIP, but the incidence light is from the opposite side of the plasmonic structure (i.e. the substrate side of the QDIP, referred to as backside-configured plasmonic structure). The excitation of the surface plasmonic waves by the backside-configured and top-configured plasmonic structures will be analyzed.

Figure 42(a) shows the cross-sectional structure of the backside configured 2DSHA plasmonic structure on the QDIP. The IR incident light illuminates from the substrate side. Figure 42(b) shows the ref-QDIP without the top plasmonic structure. The 2DSHA plasmonic structure on the QDIP and its close-up view are shown in Figure 42(c), and 42(d), respectively. As provided, square lattices are designed with the period L of 2.30 μm and the hole-diameter a of 1.15 μm, while the thickness of the deposited Au film is 25 nm.
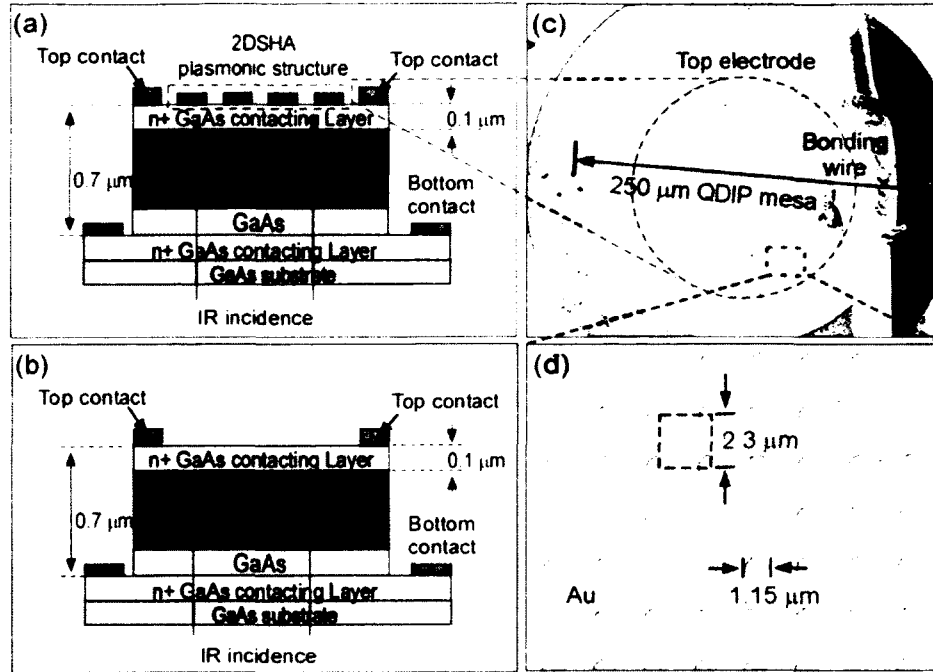
Figure 42, (a) Cross-sectional structure of the backside configured 2DSHA plasmonic structure on the QDIP. The IR incident light illuminates from the substrate side; (b) ref-QDIP without the backside plasmonic structure. (c) The 2DSHA plasmonic structure on the QDIP and (d) close-up view of the plasmonic structure.

6.1.2 Test Results

Figure 43(a) shows the measured photocurrent spectra of the QDIP with the backside configured plasmonic structure accompanied with the Ref-QDIP. In comparison, Figure 43(b) shows the photocurrent spectra of the QDIP with the top configured plasmonic structure and its reference QDIP (i.e. Ref-QDIP with top illumination). Both the top and the backside configured plasmonic structures can provide photocurrent enhancement. Visually, the backside configured plasmonic structure exhibits larger enhancement than the top configured plasmonic structure.
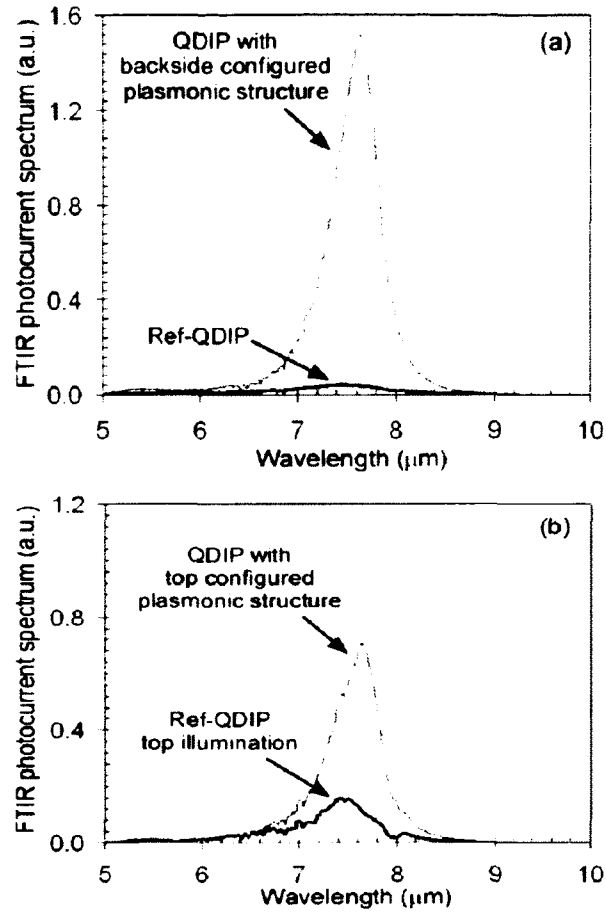
Figure 43, Measured FTIR photocurrent spectra of the QDIPs with their references: (a) backside-configured plasmonic structure and the Ref-QDIP; (b) the top-configured plasmonic structure and its reference QDIP (i.e. Ref-QDIP with top illumination).

The photocurrent of the QDIP is characterized using a (1000 K) calibrated blackbody source and a 2.4 μm long pass filter, a low-noise current preamplifier, and a fast Fourier transform (FFT) spectrum analyzer. Detailed measurement setup and procedures are described above.

Figure 44 shows the measured photocurrent of the QDIP at different bias voltages. Figure 44 (a) show the QDIP with the backside configured plasmonic structure and the Ref-QDIP. In contrast, Figure 44 (b) shows the photocurrent of the QDIP with the top configured plasmonic

structure and its reference QDIP (i.e. Ref-QDIP with top illumination). Both the top and the backside configured plasmonic structures can bring in photocurrent enhancement. The backside configured plasmonic structure exhibits about 10 times enhancement, which is larger enhancement than the top configured plasmonic structure.

Since we used 2.4 μm long pass filter in the photocurrent measurement, the 10 times enhancement is the average enhancement across the whole QDIP's detection spectrum from 4 μm to 9 μm. Because the SPR is resonant enhancement, there is no enhancement at the non-resonant wavelengths. Therefore, the average enhancement of the photocurrent is a lot less than the peak enhancement of the FTIR photocurrent spectrum.
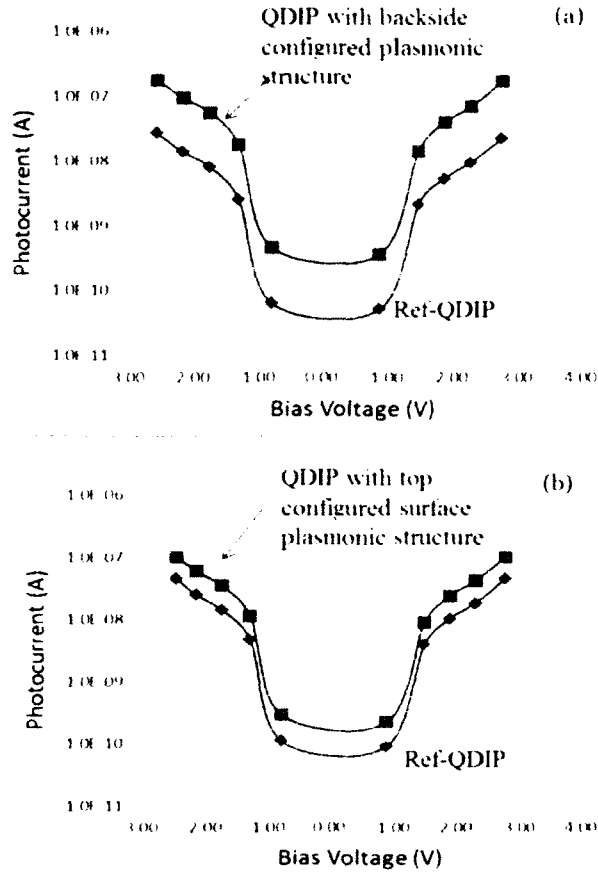
Figure 44, Measured photocurrent of the QDIPs with their references: (a) backside-configured plasmonic structure and the Ref-QDIP; (b) the top-configured plasmonic structure and its reference QDIP (i.e. Ref-QDIP with top illumination).

Figure 45 (a) and (b) show the measured noise current of the QDIP at different bias voltages for backside configuration and top side configuration. Since the QDIPs were covered with aluminum foil, no outside light shines on the sample, both the Ref-QDIP and QDIP with surface plasmonic structure show similar noise current, and both backside and top configuration show similar results.

61
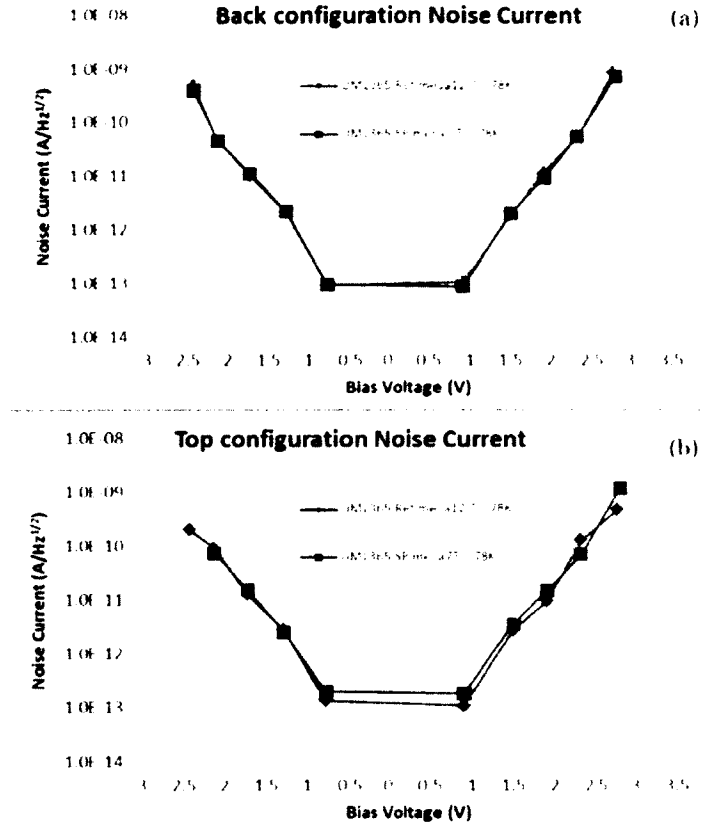
Figure 45, measured noise current of the QDIPs with their references: (a) backside-configured plasmonic structure and the Ref-QDIP; (b) the top-configured plasmonic structure and its reference QDIP (i.e. Ref-QDIP with top illumination).

Similar to noise current, the dark current shows nearly identical results for both Ref-QDIP and QDIP with surface plasmonic structure in two different cases, top and backside configuration, because there is no light source provided for the dark current measurement. Figure 46 shows the test results for the dark current density, which is defined by dark current divided by the detector's surface area.

Back configuration Dark Current Density

(a)

Top configuration Dark Current Density

(b)
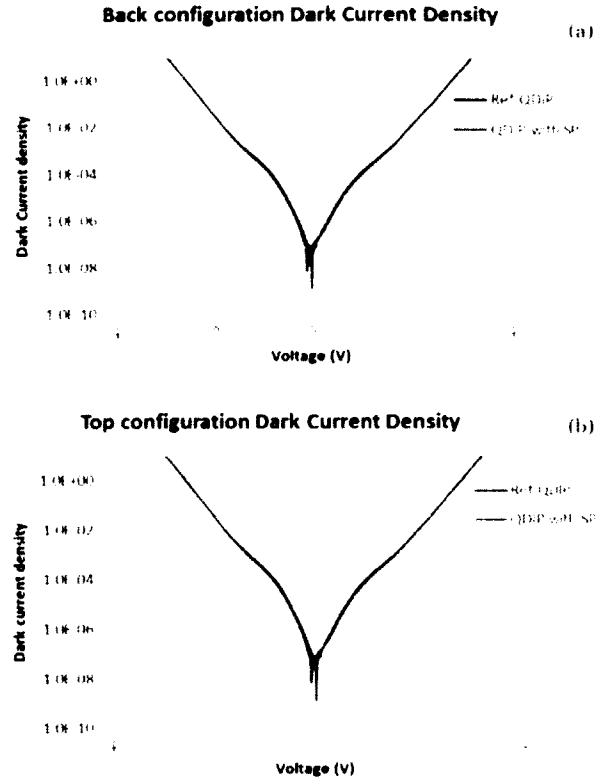
Figure 46, measured dark current density of the QDIPs with their references. (a) backside-configured plasmonic structure and the Ref-QDIP; (b) the top-configured plasmonic structure and its reference QDIP (i.e. Ref-QDIP with top illumination).

The calculated photoconductive gain from noise current and dark current is shown in Figure 47. Because of the highly similar results for noise current and dark current, it is reasonable that the similar results of the photoconductive gain were achieved for both ref-QDIP and QDIP with surface plasmonic structure at both top and backside configured situation.

Back configuratio Photoconductive Gain (a)

Top configuration Photoconductive Gain (b)
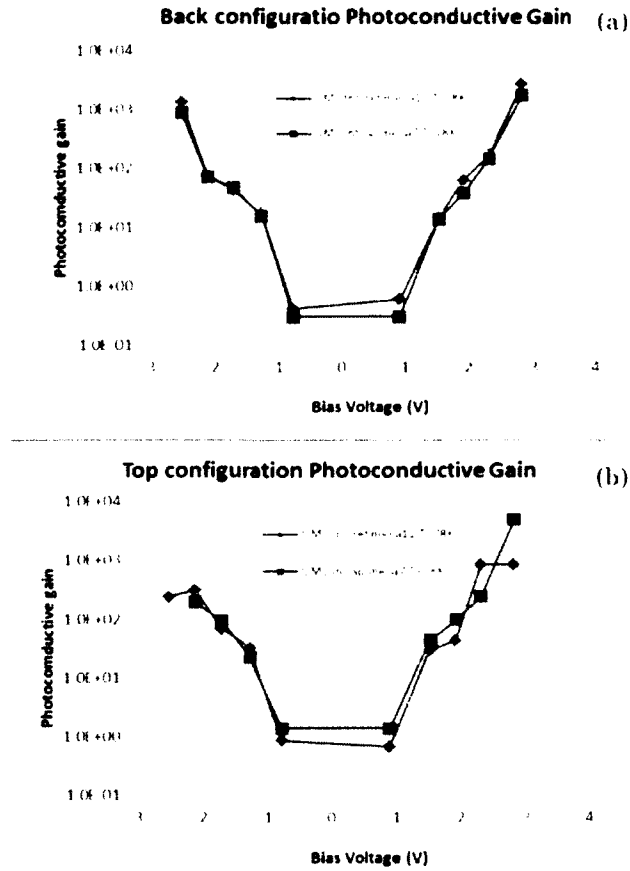
Figure 47, calculated photoconductive gain of the QDIPs with the reference(a) backside-configured plasmonic structure and the Ref-QDIP; (b) the top-configured plasmonic structure and its reference QDIP (i.e. Ref-QDIP with top illumination).

The photoresponsivity is calculated from the photocurrent, and the results are shown in Figure 48 (a) and (b) for backside and top configured plasmonic structure, respectively. The results show the same trace as the photocurrent. The backside configured plasmonic structure displays higher responsivity enhancement compared to the top configured plasmonic structure.

Back configuration Responsivity (a)

Top configuration Responsivity (b)
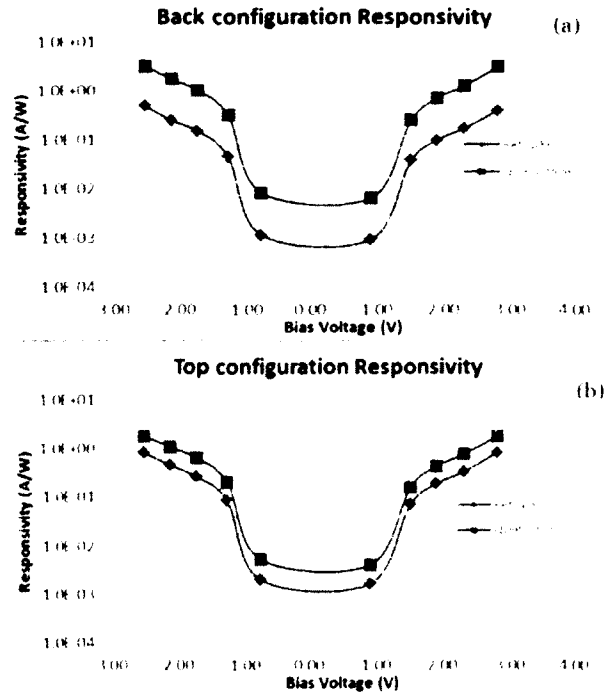
Figure 48, the calculate responsivity of the QDIP with their references: (a) backside configured surface plasmonic structure with its reference; (b) top configure surface plasmonic structure with its reference. The backside configured plasmonic structure shows higher enhancement than the top configured surface plasmonic structure.

Figure 49 (a) shows the calculated photodetectivity D^* of the QDIP with the backside-configured plasmonic structure and its ref-QDIP at different bias voltages at 77 K. A 10 times photodetectivity D^* enhancement is obtained by the backside-configured plasmonic structure. Since we used 2.4 µm long pass filter in the photodetectivity D^* measurement, the 10 times enhancement is the average enhancement across the whole QDIP's detection spectrum from 4 µm to 9 µm. As a comparison, Figure 49 (b) shows photodetectivity D^* of the QDIP with the top-configured plasmonic structure and its ref-QDIP. The backside-configured plasmonic structure can provide much higher photodetectivity D^* enhancement.
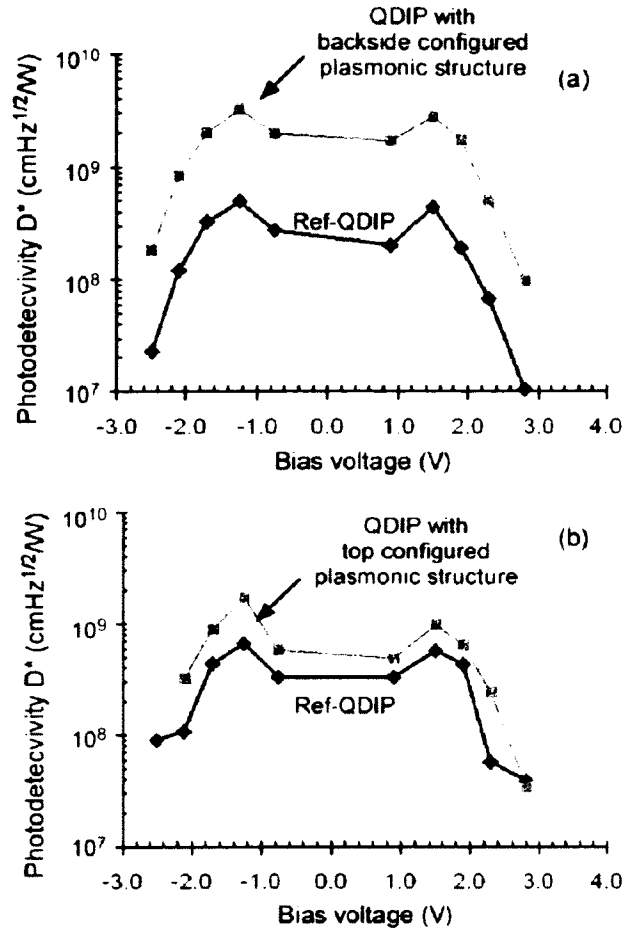
Figure 49, photodetectivity D* at different bias voltages at 77 K: (a) QDIP with the backside-configured plasmonic structure and its ref-QDIP, a 10 times D* enhancement is obtained; (b) QDIP with the top-configured plasmonic structure and its ref-QDIP, the D* enhancement is much smaller.

Figure 50 shows the quantum efficiency for the QDIP and references. Figure 50 (a) shows the calculated quantum efficiency of the QDIP with the backside-configured plasmonic structure and its ref-QDIP at different bias voltages at 77 K. By comparison, Figure 50 (b) shows quantum efficiency of the QDIP with the top-configured plasmonic structure and its ref-QDIP. The backside-configured plasmonic structure can provide much higher quantum efficiency enhancement.
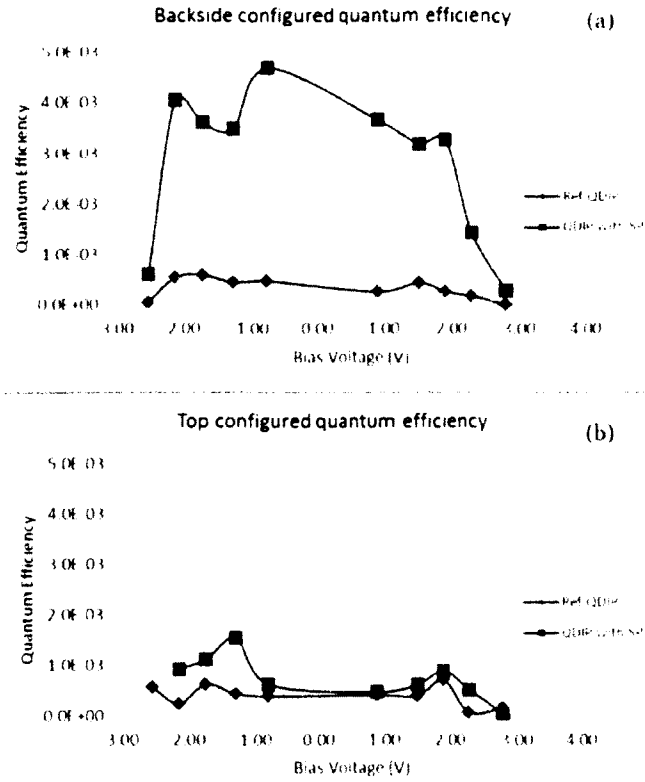
Figure 50, calculate quantum efficiency for the QDIPs with the reference: (a) backside-configured plasmonic structure and the Ref-QDIP; (b) the top-configured plasmonic structure and its reference QDIP (i.e. Ref-QDIP with top illumination).

6.1.3 Analysis and Discussion

The enhancement factor can be defined as the photocurrent ratio between the plasmonic enhanced QDIP and its Ref-QDIP. Figure 51 shows the comparison of the enhancement factors of the top and the backside configured plasmonic structures. The backside configured plasmonic structure provides an over 40 times peak enhancement factor with a wide enhancement spectral width (FWHM) of ~ 0.7 μm, whereas the top configured plasmonic structure only shows a peak enhancement factor of 7.6 times with a much narrow spectral width (FWHM) of 0.4 μm.

50.0

40.0

30.0

20.0

10.0

0.0

Enhancement spectrum

QDIP with backside configured plasmonic structure

FWHM |- - -|

QDIP with top configured plasmonic structure

FWHM

5   6   7   8   9   10

Wavelength (μm)
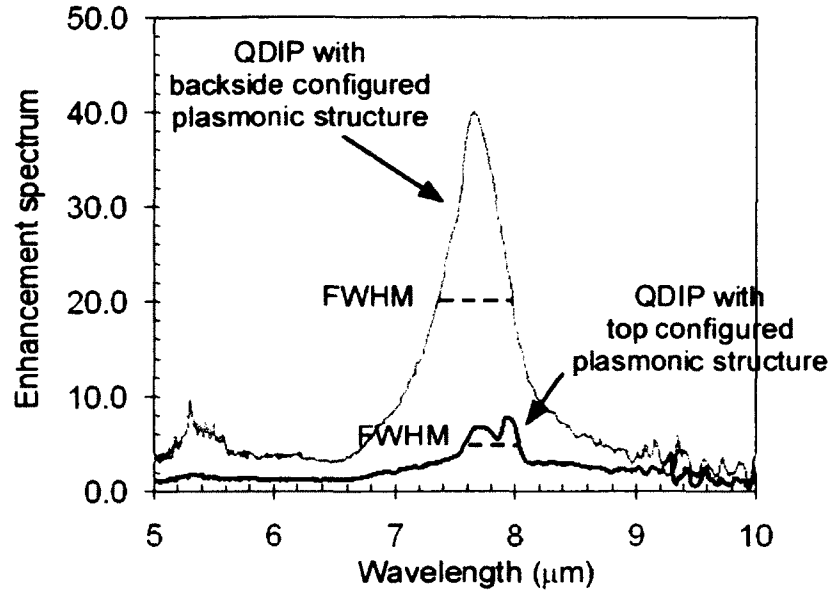
Figure 51, Photocurrent enhancement ratio of the backside-configured and top-configured plasmonic structures. An over 40 times peak photocurrent enhancement is obtained by the backside-configured plasmonic structure.

To understand the difference in enhancement by the top- and backside- configured plasmonic structures, we analyze the coupling of the plasmonic resonant waves for both configurations, as shown in Figure 52. The plasmonic structures have two interfaces, i.e the air/metal and the semiconductor/metal interfaces. The plasmonic resonant wavelength λ_{sp} at the air/metal and the semiconductor/metal interfaces is analyzed in Eq(2.4)

$$\lambda_{sp} = \frac{d}{\sqrt{i^2 + j^2}} \text{Re}\left\{ \left[\frac{\varepsilon_m \varepsilon_d}{\varepsilon_m + \varepsilon_d} \right]^{1/2} \right\},$$

As mentioned before, d is the period of the holes, (i, j) are the orders of the grating vectors, ε_m and ε_d are the relative permittivities of the metal and dielectric (i.e. air or semiconductor), respectively. The plasmonic resonant wavelengths λ_{sp} are quite different on the air/metal and the semiconductor/metal interfaces due to the large difference between the relative

68

permittivities of the air and semiconductor (GaAs). Since the QDIP is on the semiconductor side, the excitation of the plasmonic wave on the metal/semiconductor side is more important for the plasmonic enhancement.
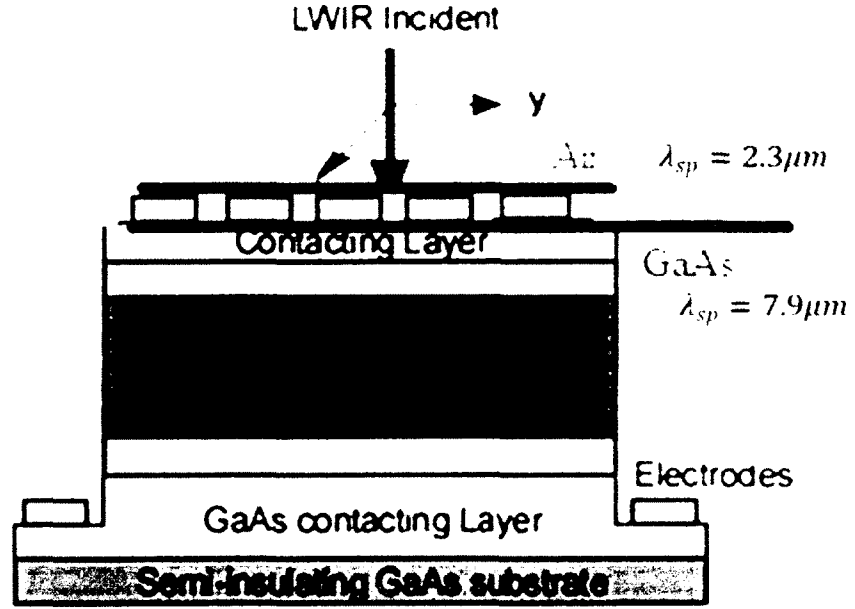
Figure 52, the coupling of the plasmonic resonant waves for top configuration. The plasmonic structures have two interfaces, i.e the air/metal and the semiconductor/metal interfaces. The resonant wavelengthes at these two interfaces are 2.3um and 7.9um respectively.

For the top-configured plasmonic structure, the IR incidence is from the air/metal interface, the plasmonic wave excited at the air/metal interface has a resonant wavelength of ~ 2.3 μm, which is beyond the detection spectrum of the QDIP and thus is not a wavelength of interest. The plasmonic wave excited at the metal/semiconductor interface has a resonant wavelength of ~ 7.9 μm, which is within the detection spectrum of the QDIP.

Figure 53 shows the simulated transmission (solid line) and reflection spectra (dashed line) of the metallic 2DSHA plasmonic structures using CST's simulation software: (a)

Top-configured; (b) backside-configured. The top- and the backside-configured plasmonic

structures show the same transmission, but the reflection of the backside-configured plasmonic

structure is much less than that of the top-configured plasmonic structure. The same

transmission with lower reflection indicates higher plasmonic excitation for the

backside-configured plasmonic structure. The transmission spectrum also shows two resonant

peaks at 7.9 μm and 5.6 μm, corresponding to the plasmonic wave at the metal/GaAs interface

with (i=1, j=0) or (i=0, j=1), and (i=1, j=1) in Eq. (2.4), respectively.
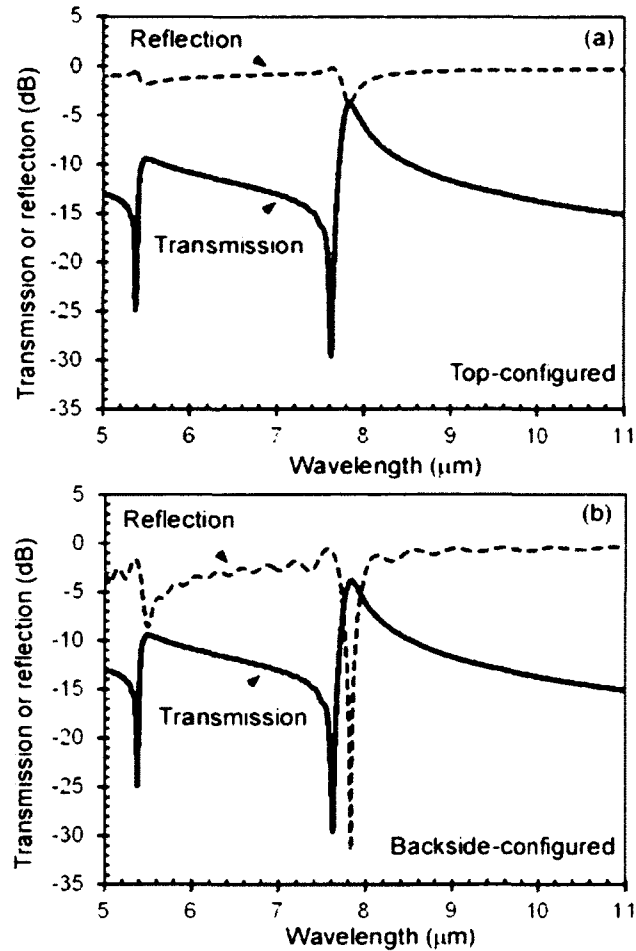
Figure 53, simulated transmission spectrum of the metallic 2DSHA plasmonic structure using CST's simulation software. The Enhancement Ratio is correspond to the transmission spectrum, and the resonant wavelength shift is explained in previous work[36].

For the top configured plasmonic structure, the excitation of the plasmonic wave on the metal/semiconductor side is the evanescence waveguide modes through the subwavelength hole array[39, 44]. The intensity of the plasmonic wave on the metal/semiconductor side is therefore dependent on the intensity of the evanescent modes at the output side (i.e. at metal/semiconductor interface). The decay of the evanescence wave is determined by the wave vector component along the z-direction $k_{m,z}$ of the evanescent waveguide modes, i..e

$$P_m(d) = P_m(0)\exp(-2|k_{m,z}|d),$$
(6.1)

where, m indicates the order of the modes, and $P_m(0)$ and $P_m(d)$ are the intensity of the evanescence modes at the input side (i.e. air/metal interface) and output side (metal/semiconductor interface), respectively. $k_{m,z}$ is related to the radical (parallel to the surface) field component E_ρ distribution parameter $\beta_{m,\rho}$ by :

$$k_{m,z}^2 = k_0^2 - \beta_{m,\rho}^2$$
(6.2)

where, $k_0 = 2\pi/\lambda_{sp}$ in the hole. $\beta_{m,\rho}$ is determined by the boundary conditions at the air/metal interface in the holes.

To verify the above analysis, we simulated the E-field distribution. Figure 54 shows the comparison of the E-filed distribution by the top and the bottom illumination, respectively. From the top illumination (Figure 54 a), the E-field decays as it passes through the holes and the SPR is excited by the evanescent mode through the hole. This agrees with Eq. (6.1). From the bottom illumination, the E-field does not experience evanescent decay through the hole (Figure 54 b). The SPR is excited directly by the incident light.
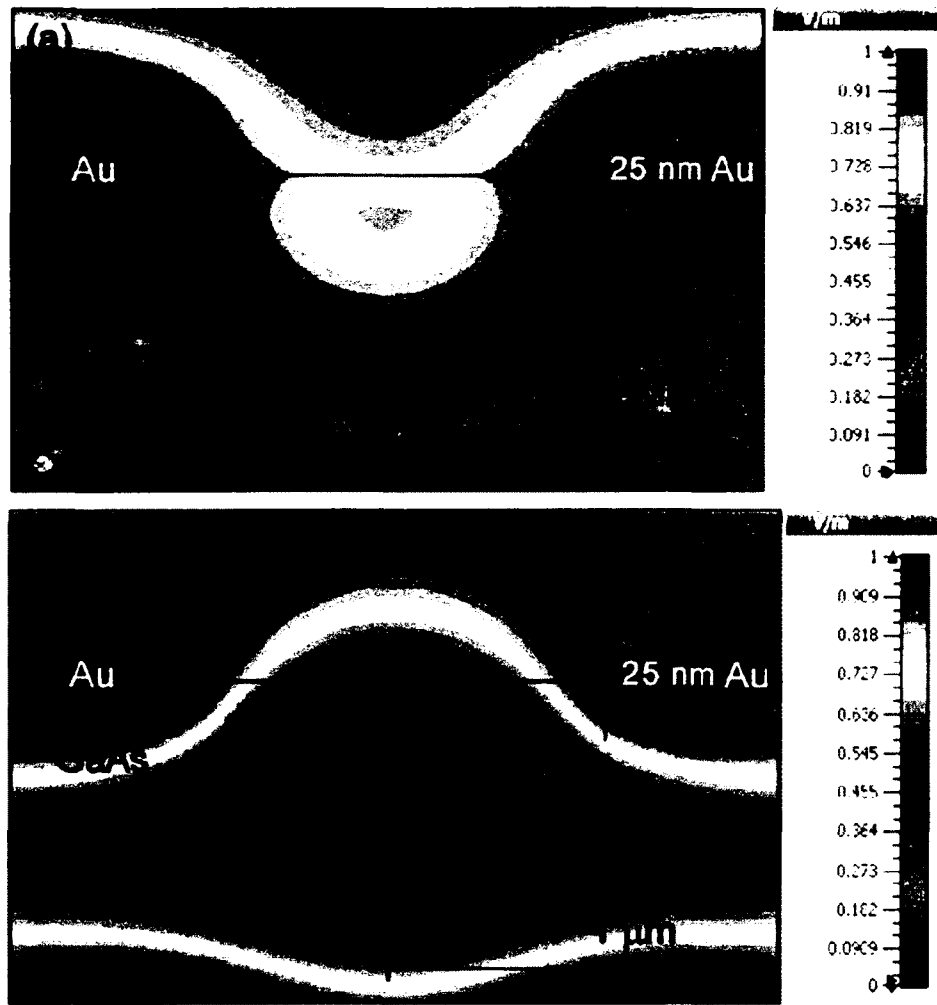
Figure 54, Comparison of the simulated the E-field distribution from top illumination (a) and from the bottom illumination (b).

Nevertheless, for the top-configured plasmonic structure, the excitation of the plasmonic wave at the metal/semiconductor is not efficient due to the evanescent decay of the evanescent modes through the subwavelength holes.

For the backside-configured plasmonic structure, however, the plasmonic resonance is directly excited at the semiconductor/metal surface. The excitation efficiency is much larger than that of the top configured plasmonic structure where the plasmonic wave excitation is

excited by the evanescent modes through the subwavelength holes. Due to the higher excitation efficiency, the plasmonic resonance is stronger in the backside-configured plasmonic structure. This partially explains the higher enhancement in the backside-configured plasmonic QDIP.

Note that the backside-configured plasmonic structure is not optimized. Higher enhancement can be expected by optimizing the backside-configured plasmonic structure (e.g. reducing the loss by increasing the metal thickness, employing localized surface plasmonic resonance, and the thickness of the substrate for Fabre-Perot cavity effect) and improving excitation efficiency of the plasmonic waves.

In conclusion, we measured and compared the QDIP enhancement by the backside- and top- configured plasmonic structures. The backside configured plasmonic structure can provide much higher photocurrent and photodetectivity D^* enhancement. Furthermore, we analyzed the excitation of the surface plasmonic waves by the backside- and top- configured plasmonic structures. Higher enhancement is mainly attributed to its higher efficiency. In particular, an over 40 times peak photocurrent enhancement is obtained by the backside-configured plasmonic structures. Higher enhancement is expected by optimizing the backside-configured plasmonic structure and improving excitation efficiency of the plasmonic waves.

6.2 Investigate other types of back configured plasmonic structures

6.2.1 Introduction

Metallic two-dimensional (2D) subwavelength hole array (2DSHA) plasmonic structures show extraordinary transmission and have been extensively applied to improve the performance of QDIPs, which was illustrated in last project. Nevertheless, since the extraordinary transmission only shows up at the plasmonic resonance wavelength, the transmission off the plasmonic resonant wavelength is significantly blocked by the metallic film. This fact has become an obstacle for the development of broadband photodetcors with vertically stacked multiple absorption regions. In this project, a QDIP enhanced by localized surface plasmonic resonance (LSPR) in a metallic subwavelength circular disk array will be investigated. The performance enhancement by the LSPR in the subwavelength circular disk array is measured by both top configuration and backside configuration, which is identical to the 2DSHA performance test. The comparison results between the 2DSHA and LSPR enhancements will be discussed.

The localized surface plasmonic structure circular disk array (dots array) is fabricated on sample UML365, the same as last project. Information about the sample was provided in the previous sections. The dot diameter is 1.15um and the period is 2.3um which is written by E-beam lithography. Figure 55 (a) shows the Ref-QDIP without any surface plasmonic structure on it, Figure 55 (b) shows QDIP with dots array surface plasmonic structure on it,

and (c) is the close-up view of the dots array. The dot's diameter is 1.15um, period is 2.3um and the metal thickness is 25nm.
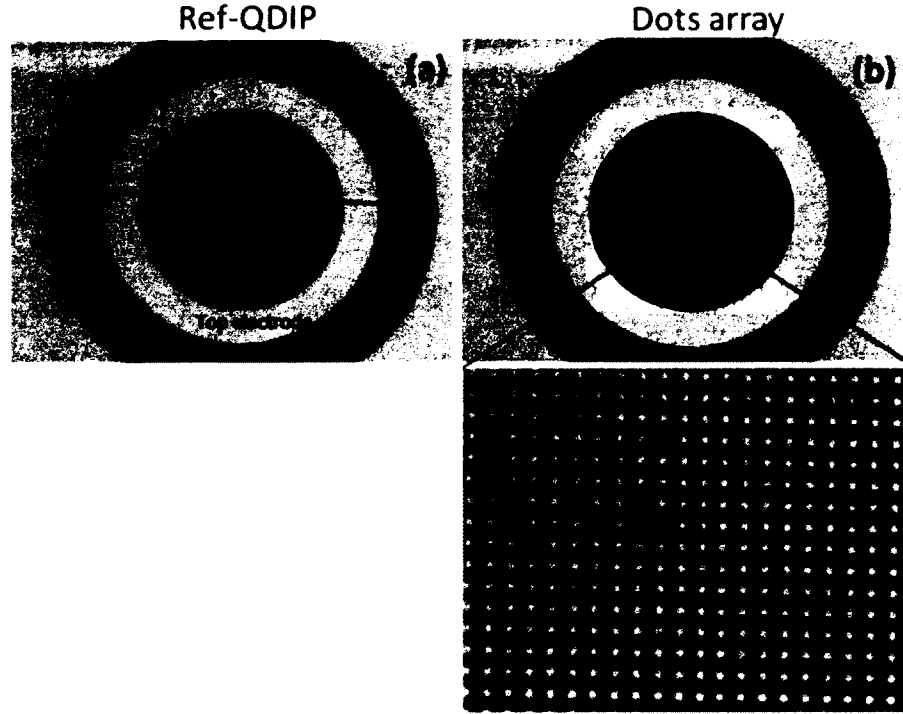
Figure 55(a)ref-QDIP without the plasmonic structure. (b) The 2DSHA plasmonic structure on the QDIP and (c) close-up view of the plasmonic structure.

6.2.2 Test Results

Figure 56(a) shows the measured photocurrent spectra of the QDIP with the backside configured localized surface plasmonic structure (dots array) and the Ref-QDIP. In comparison, Figure 43(b) shows the photocurrent spectra of the QDIP with the top configured plasmonic structure and its reference QDIP (i.e. Ref-QDIP with top illumination). Both the top and the backside configured plasmonic structures can provide photocurrent enhancement. Although the peak point of the FTIR is similar for the top and backside configuration, the

backside configured plasmonic structure exhibits larger enhancement than the top configured

plasmonic structure, because the reference QDIP getting smaller.

Backside configuration FTIR (a)

Top Configuration FTIR (b)
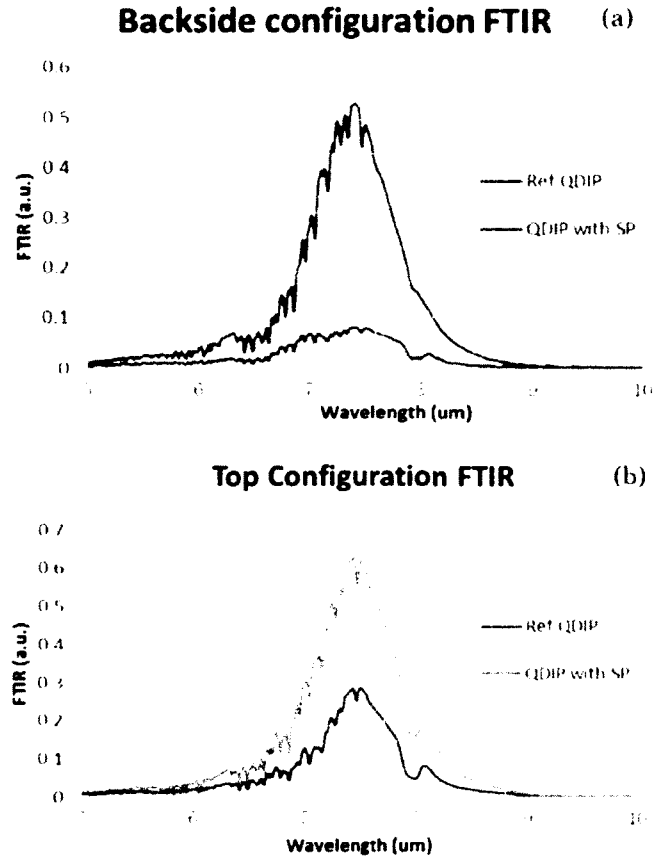
Figure 56 FTIR photocurrent spectrum test results for the Ref-QDIP and QDIP with dots array plasmonic structure on it (a) backside configured surface plasmonic structure FTIR photocurrent spectrum and (b) top configured surface plasmonic structure FTIR photocurrent spectrum

Similar to the 2DSHA test, the noise current and the black current provide close results,

whereas the aluminum foil on the sample blocked the light. Therefore, the photoconductive

gain derived from the noise and dark currents also presents similar results for both Ref QDIP

and QDIP with LSPR in the case of top and backside configurations.

In the same way, the photocurrent is tested by blackbody source, preamplifier and the FFT

spectrum analyzer. Figure 57 shows the measured photocurrent of the QDIP at different bias voltages with (a) about backside configured LSPR and its Ref-QDIP and (b) about to configured LSPR and its reference. As expected, the backside configured structure provided more distinct enhancement on the signal than the top configured one.

It is explained that the FTIR photocurrent spectrum has much higher enhancement compared the photocurrent results for 2DSHA because the FTIR is peak enhancement, while the photocurrent is average enhancement, but for the LSPR, the FTIR enhancement comparable to the photocurrent enhancement.

Backsid Configuration Photocurrent (a)

Top Configuration Photocurrent (b)
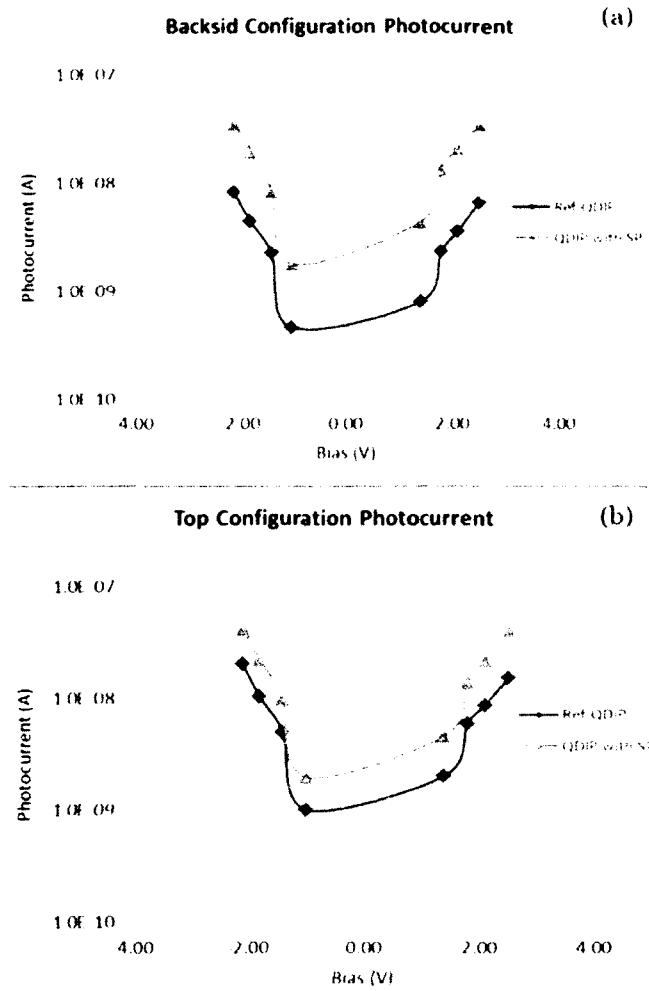
Figure 57 Photocurrents of the Ref-QDIP and the QDIPs with the top- and backside-configured LSPR structures at different biases: (a) backside-configured LSPR structure; (b) top-configured LSPR structure.

The photoresponsivity of the QDIPs with backside- and the top-configured LSPR plasmonic structures at different bias voltages are presented in Figure 58(a) and Figure 58(b), respectively. The photoresponsivity v.s. bias traces are very similar to those of the photocurrent v.s bias traces shown in Figure 57. This is due to the same magnitudes of power from the incident light are received for all detectors. For the same reason presented in Section

6.1.3, the backside-configured LSPR structure provides higher photoresponsivity enhancement.

Backside Configured Photoresponsivity (a)

Top Configured Photoresponsivity (b)
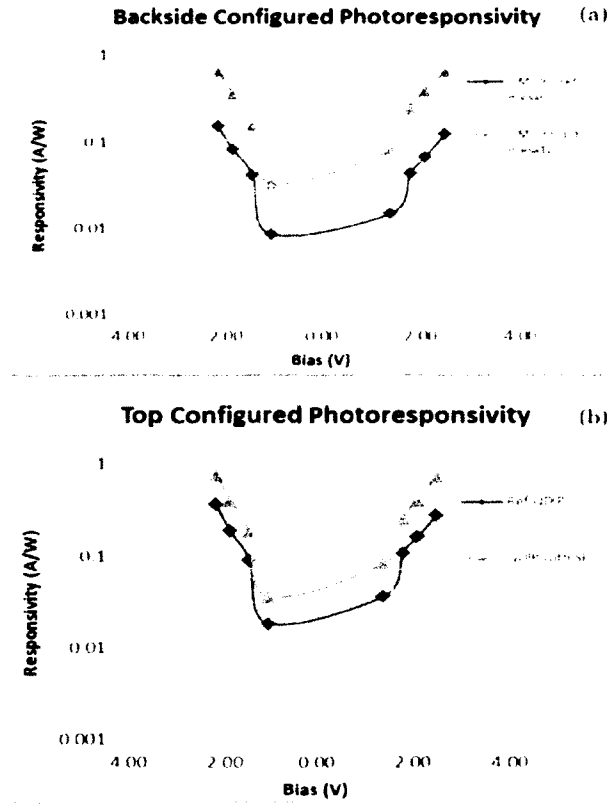
Figure 58, Calculated photoresponsivity for the QDIP with LSPR and the reference in both backside configuration and backside configuration. (a) backside configured LSPR photoresponsivity and (b) top configured LSPR photoresposivity

The photodetectivity D^* of the backside-configured and the top-configured plasmonic structure enhanced QDIPs are shown in Figure 59(a) and (b), respectively. Higher photodetectivity enhancement by the backside-configured structure is clearly observed. To block the photocurrent from the short wave IR light, a 2.4 μm long pass filter was used in the photodetectivity D^* measurement. Since the measured photocurrents are the total photocurrents from the whole QDIP's detection spectrum from 4 μm to 9 μm, the

79

photodetectivity enhancements are also the average enhancement of the whole QDIP's

detection spectrum.
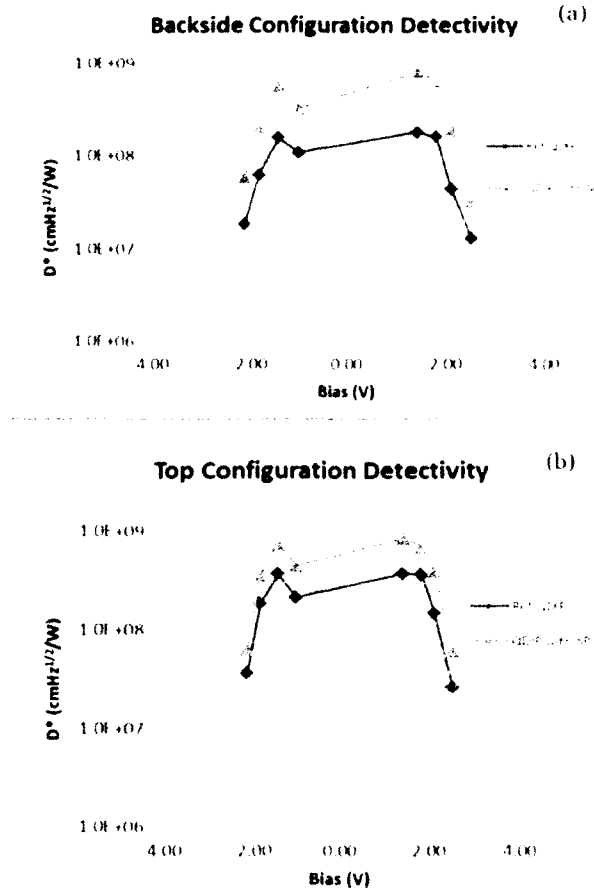
Figure 59, Calculated photodetectivity of the QDIP with LSPR and it's references. (a) Backside configured LSPR detectivity and (b) top configured LSPR detectivity.

6.2.3 Analysis and Discussion

1. Backside configured LSPR enhancement

Taking over the previously defined enhancement factor, which is the ratio of the

photocurrent the plasmonic enhanced QDIP over its Ref-QDIP, I obtain the enhancement

factors of the top- and the backside-configured LSPR structures. Figure 60 shows the comparison of the enhancement factors of the top- and the backside- configured LSPR structures. As seen apparently, the backside-configured LSPR structure shows a higher enhancement ratio in comparison with the top configured LSPR structure.

FTIR Enhancement Ratio
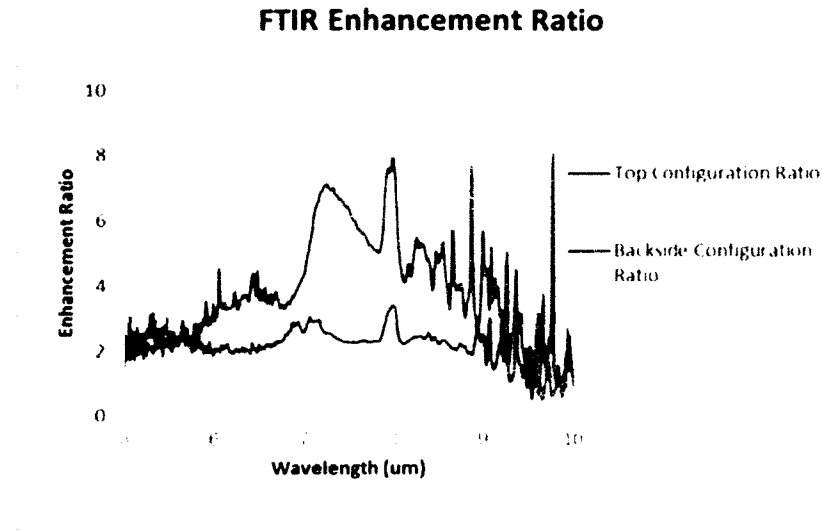
Figure 60, Enhancement Ratio of the top and backside configuration, the backside configured LSPR shows higher enhancement ratio compared with top configured LSPR

As shown in the previous section 6.1.3, the backside-configured plasmonic structure can provide much higher plasmonic excitation efficiency than the top-configured plasmonic structure. To check whether this is still valid for the LSPR structures, I conducted E-field distribution simulation for both the backside- and top-configured LSPR structures.

Figure 61 compares the E-field distributions of the backside- and top-configured LSPR structures. Figure 61 (a) shows the E-field distribution of the backside-configured LSPR structure, and Figure 61 (b) illustrates that of the backside-configured LSPR structure. As shown in Figure 61 (a) and (b), the E-field distribution of the back-configured LSPR structure

(Figure 61(a)) is much stronger than that of the top-configured LSPR structure (Figure 61(b)).

The stronger E-field distribution indicates that the backside configured LSPR structure can

provide higher SPR excitation efficiency. Due to the higher SPR excitation efficiency, the

plasmonic enhancement becomes stronger in the backside-configured plasmonic structure.

This partially explains the higher enhancement in the backside-configured plasmonic QDIP.
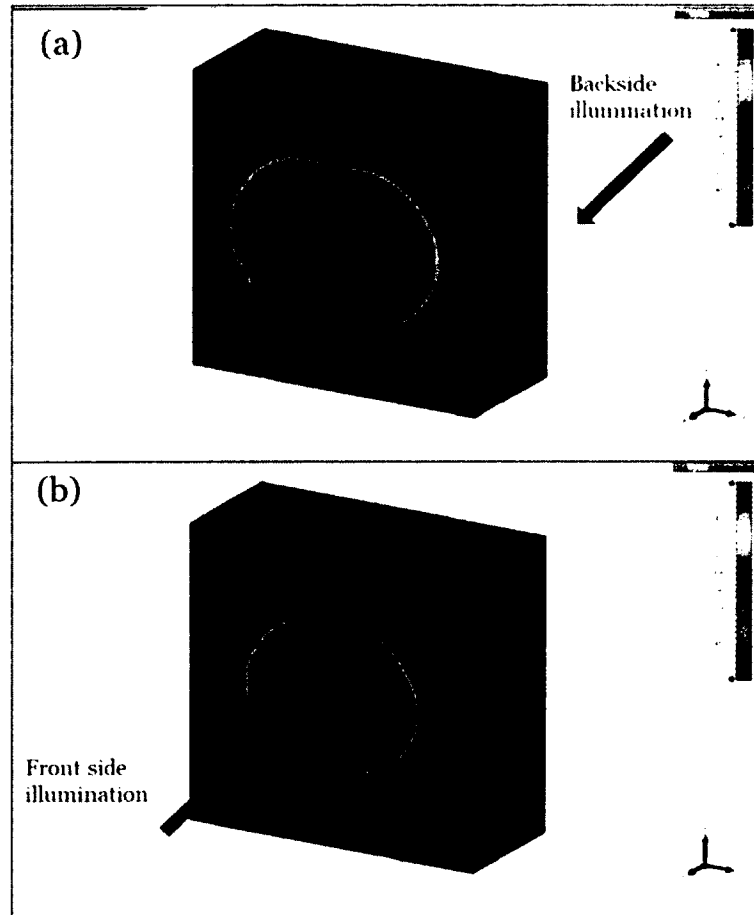
Figure 61 the comparison of the E-filed distribution by the backside and the front side illumination, respectively. (a) E-filed distribution for backside illumination; (b) E-filed distribution for front side illumination.

2. LSPR and 2DSHA enhancement comparison

To evaluate and compare the 2DSHA and the LSPR enhancement on the QDIPs, both hole and dots array structures are fabricated on the surface of the regular QDIP by E-beam lithography at the same time. Figure 62 gives the microscope figures and SEM images of QDIPs fabricated with dots and hole array structures. Figure 62(a) shows the Ref-QDIP without any plasmonic structure attached; Figure 62(b) illustrates the SEM image of the overview of QDIPs with bonding wires, including column 1 QDIPs with dots array, column 2 QDIPs with hole array, column 3 and column 4 QDIPs as references without any plasmonic structures on; Figure 62 (c) presents QDIP with hole array on the top of the surface; Figure 62 (d) is the SEM image of close-up view of the holes with 1.15um diameter and 2.3um period; Figure 62 (e) gives image of the QDIP with dots array; and finally Figure 62 (f) shows the SEM image of the zoomed in view of the dots with 1.15um dots diameter and 2.3um hole size.
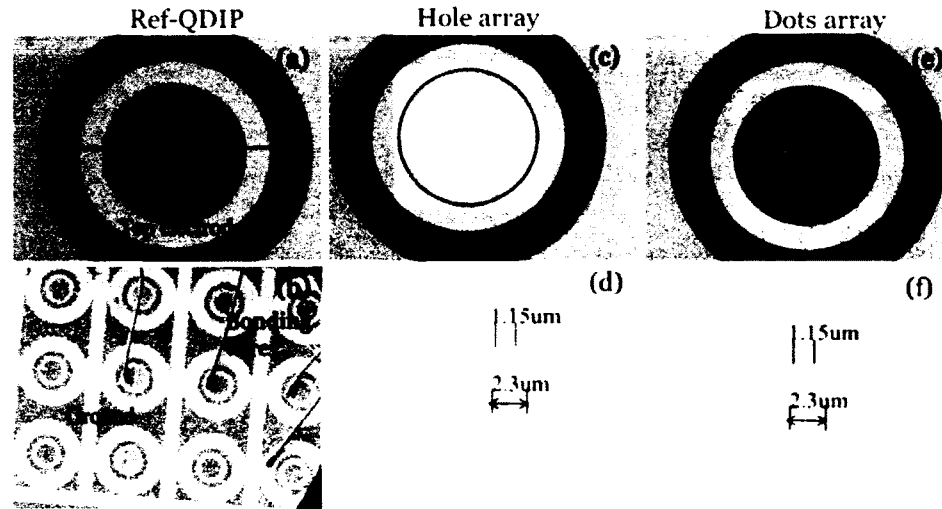
Figure 62 Microscope figures and SEM images of QDIP with dots and hole array (a) Ref-QDIP without any plasmonic structure on it; (b) the SEM image of the overview of QDIPs with bonding wires, the column 1 with dots array, column 2 with hole array, column 3 and column 4 are references; (c) QDIP has hole array on the top of the surface; (d) the SEM image of close-up view of the holes with 1.15um diameter and 2.3um

period; (e) QDIP with dots array; and (f) the SEM image of zoomed in view of the dots with 1.15um dots diameter and 2.3um hole size.

Figure 63 shows FTIR photocurrent spectra test results for QDIP with LSPR and 2DSHA structures, and the references. Both backside (Figure 63 (a)) and top (Figure 63(b)) configurations show that the 2DSHA has higher enhancement.
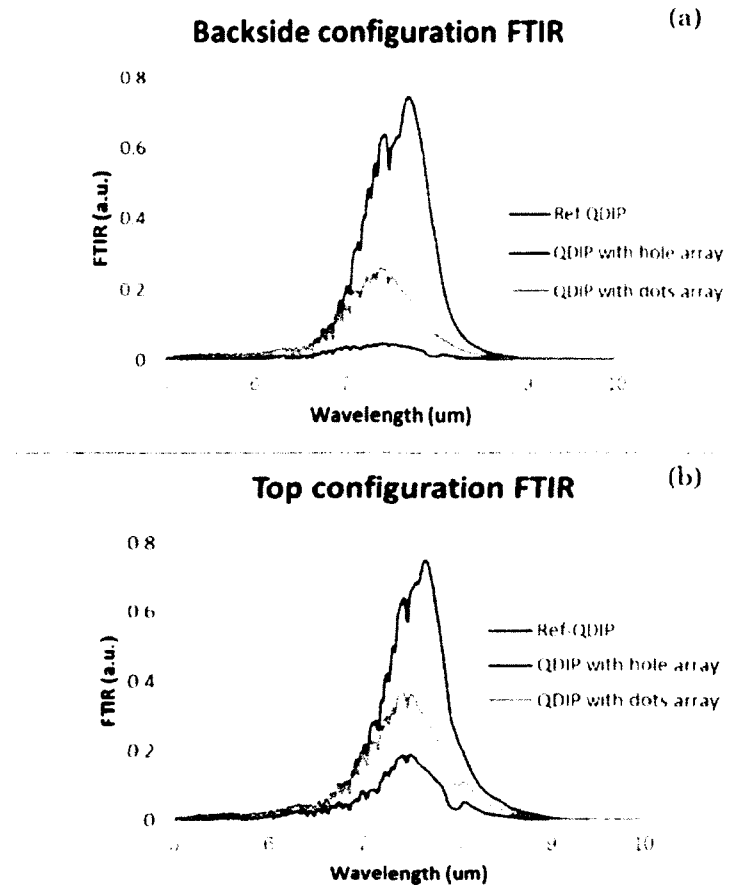
Figure 63 FTIR photocurrent spectra test results for QDIP with LSPR and 2DSHA structures and the references. (a) backside configuration; (b) top configuration. Both backside and top configurations show that the 2DSHA has higher enhancement.

Figure 64 shows the FTIR photocurrent spectra enhancement ratio and the photocurrent enhancement ratio at different bias voltages for both LSPR and 2DSHA structures. Figure 64 (a) and (b) show the FTIR photocurrent spectra and photocurrent enhancement ratio for the LSPR , respectively. In comparison, Figure 64 (c) and (d) illustrate the results of 2DSHA enhancement ratio for FTIR and photocurrent, respectively. Intuitively, the 2DSHA provides much higher FTIR enhancement compared to the LSPR. However, the LSPR's photocurrent enhancement ratio is comparable to 2DSHA's.
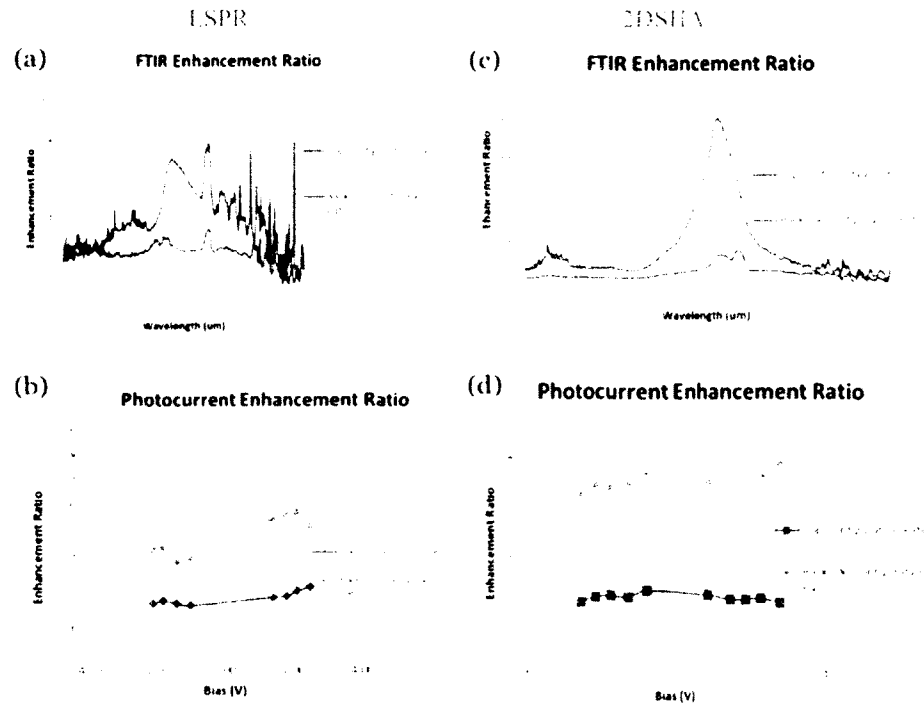
Figure 64 FTIR photocurrent spectra and the photocurrent at different bias voltages enhancement ratio for both LSPR and 2DSHA structures. Figure 64 (a) and (b) show the FTIR photocurrent spectra and photocurrent enhancement ratio for the LSPR, respectively; (c) and (d) show the 2DSHA enhancement ratio of FTIR and photocurrent, respectively.

To demonstrate the different enhancement results for the LSPR and 2DSHA plasmonic structures, simulations of the transmission spectra of both plasmonic structures are performed using CST software, and simulation results we obtained out are shown in Figure 65. As seen from the figure, for the 2DSHA (the black curve), the extraordinary transmission only shows up at the plasmonic resonance wavelength, while the transmission off the plasmonic resonant wavelength is significantly blocked by the metallic film. Because of this, the 2DSHA can provide much higher enhancement at the resonant wavelength point as shown in the FTIR enhancement ratio, but the average enhancement photocurrent ratio over the whole photodetector spectrum is much lower than the peak resonant enhancement ratio. However, for the LSPR structure (the red curve), as seen from the transmission spectrum, the light passes through most of the wavelength and the off-resonant wavelengths are not blocked by the LSPR structure. Therefore, the average photocurrent enhancement factor is comparable to that at the peak resonant wavelength.
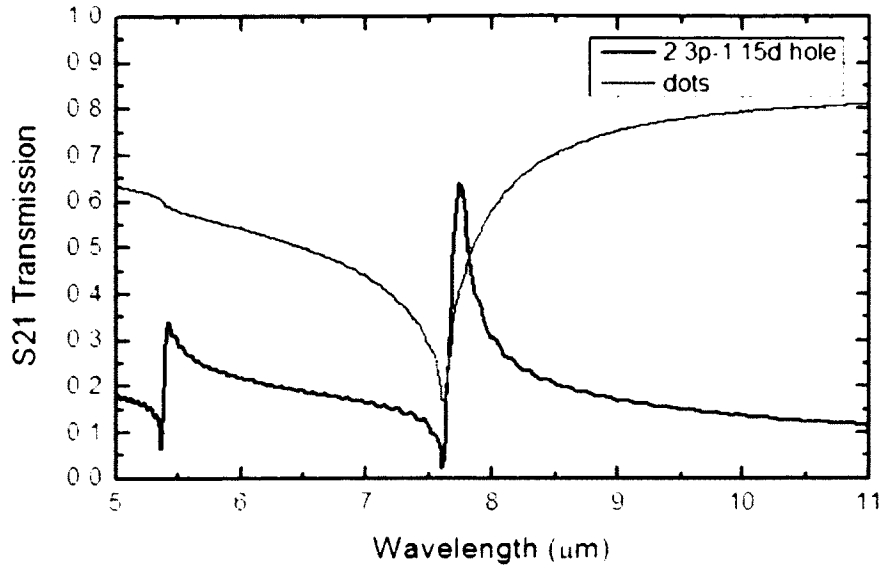
Figure 65 Simulation transmission spectra for both LSPR and 2DSHA plasmonic structures using CST's simulation software. The red curve is for LSPR and the black one is for the 2DSHA, respectively.

In conclusion, the QDIPs enhanced by the backside- and top- configured localized plasmonic structures are measured and compared. The backside configured plasmonic structure can provide higher photocurrent and photodetectivity D^* enhancement. The excitation of the localized surface plasmonic waves by the backside- and top- configured plasmonic structures is analyzed. Higher enhancement is mainly attributed to its higher efficiency. The 2DSHA and LSPR enhancements on QDIP are evaluated and compared. The 2DSHA give much higher peak photocurrent enhancement, while the LSPR has similar enhancement for the peak photocurrent and average photocurrent enhancement. The reason for the different results is future analyzed.

6.3 Metal Thickness Effect

6.3.1 Introduction

In order to further improve the efficiency of the plasmonic excitation for higher device performance enhancement and pursue deep understanding of the evanescent modes, the plasmonic loss and their roles in the plasmonic enhancement, the 2DSHA plasmonic structures with different metal thickness was fabricated and the top- and backside configured enhancements for the QDIP performance were measured and compared. The relationship between the metal thickness and the enhancement is further analyzed.

The sample used in this project is UML291, and the FTIR performance of the sample at different bias is shown in Figure 66.
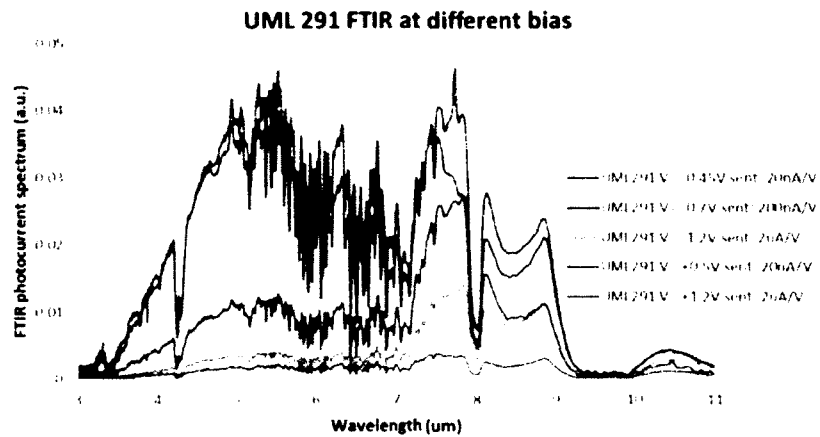
Figure 66, The FTIR photocurrent spectrum of sample UML291 at different bias.

Since this sample has very wide spectrum ranging from 3um to 11um, we picked up the 2DSHA plasmonic structure with period of 2.4um, hole size of 1.2um, and the metal thickness

of 25nm, 50nm, 75nm, and 100nm, respectively. The plasmonic structure is fabricated by regular photolithography, metal deposition and lift off processes. After the fabrication, the backside substrates of the samples are polished and mounted on the copper plates with holes as mentioned in Chapter4 to prepare for the further test.

6.3.2 Test Results

Figure 67 shows the top- and backside-configured FTIR photocurrent spectra enhancement ratio with different metal thicknesses. Figure 67 (a), (b) (c) and (d) show enhancement factors for metal thicknesses of 25nm, 50nm, 75nm, and 100nm respectively. All the figures prove that the backside-configured 2DSHAs have higher enhancement ratio compared with the top-configured surface plasmonic structure, which agree with and further prove the previous results. Also, one can notice that, the enhancement factor increase from ~40 (25nm) to ~60 (75nm), which means that by increasing the metal thickness one can increase the enhancement factor.

UML291 SP2.4_1.3 Au 25nm   (a)   UML291 SP2.4_1.3 Au 50nm   (b)

UML291 SP2.4_1.3 Au 75nm   (c)   UML291 SP2.4_1.3 Au 100nm   (d)
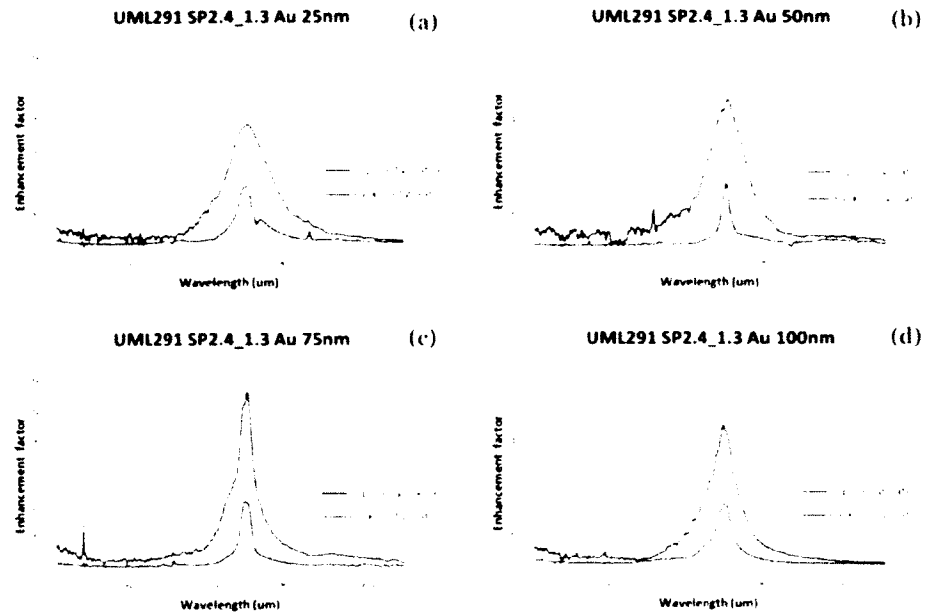
Figure 67, Top- and backside-configured SPR enhancement factors with different metal thickness. (a), (b), (c) and (d) show the enhancement factor for metal thickness of 25nm, 50nm, 75nm and 100nm, respectively.

6.3.3 Analysis and Discussion

To further observe the metal thickness effect on the device performance enhancement, all the enhancement factors with different metal thicknesses are rearranged for the top- and backside- configured plasmonic structure as shown in Figure 68. We found that not only the plasmonic enhancement is related to the metal thickness, but also the spectral width of the plasmonic enhancement also depends on the metal thickness.

90

Back configured enhancement factor (a)

Top configured enhancement factor (b)
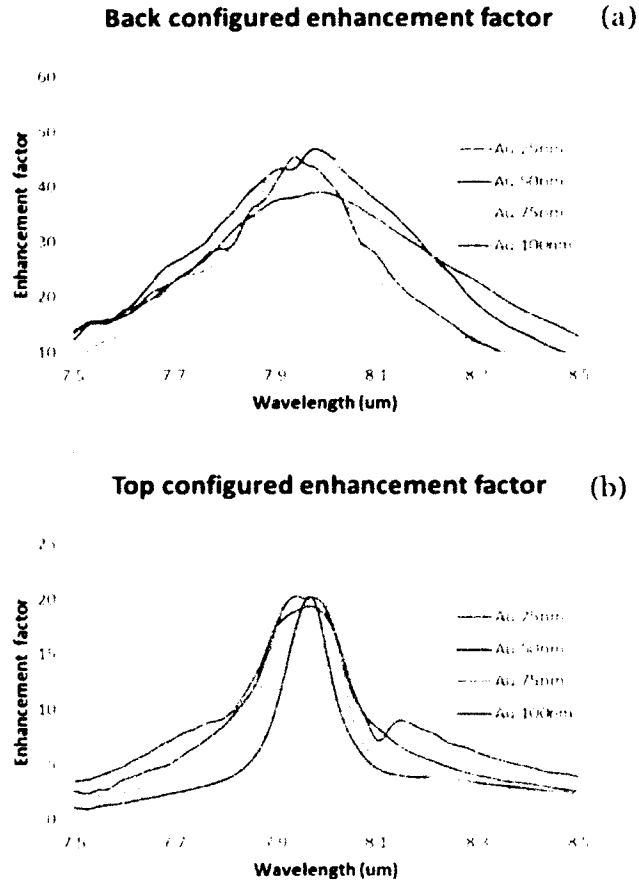
Figure 68, (a) backside-configured enhancement factors with different metal thickness; (b) top-configured enhancement factors with different metal thickness.

Simulations were performed to further analyze the metal thickness effect. Figure 69 shows the simulated transmission (dashed lines) and reflection spectra (solid lines) of the metallic 2DSHA plasmonic structures using CST's simulation software: (a) backside-configured; (b) top-configured. The same transmission was presented in the top- and the backside-configured plasmonic structures, but the reflection of the backside-configured plasmonic structure is much less than that of the top-configured plasmonic structure for all the metal thicknesses. The same transmission with lower reflection indicates higher plasmonic

excitation for the backside-configured plasmonic structure. The higher plasmonic excitation

leads to a higher enhancement factor for the backside-configured plamonic structure as shown
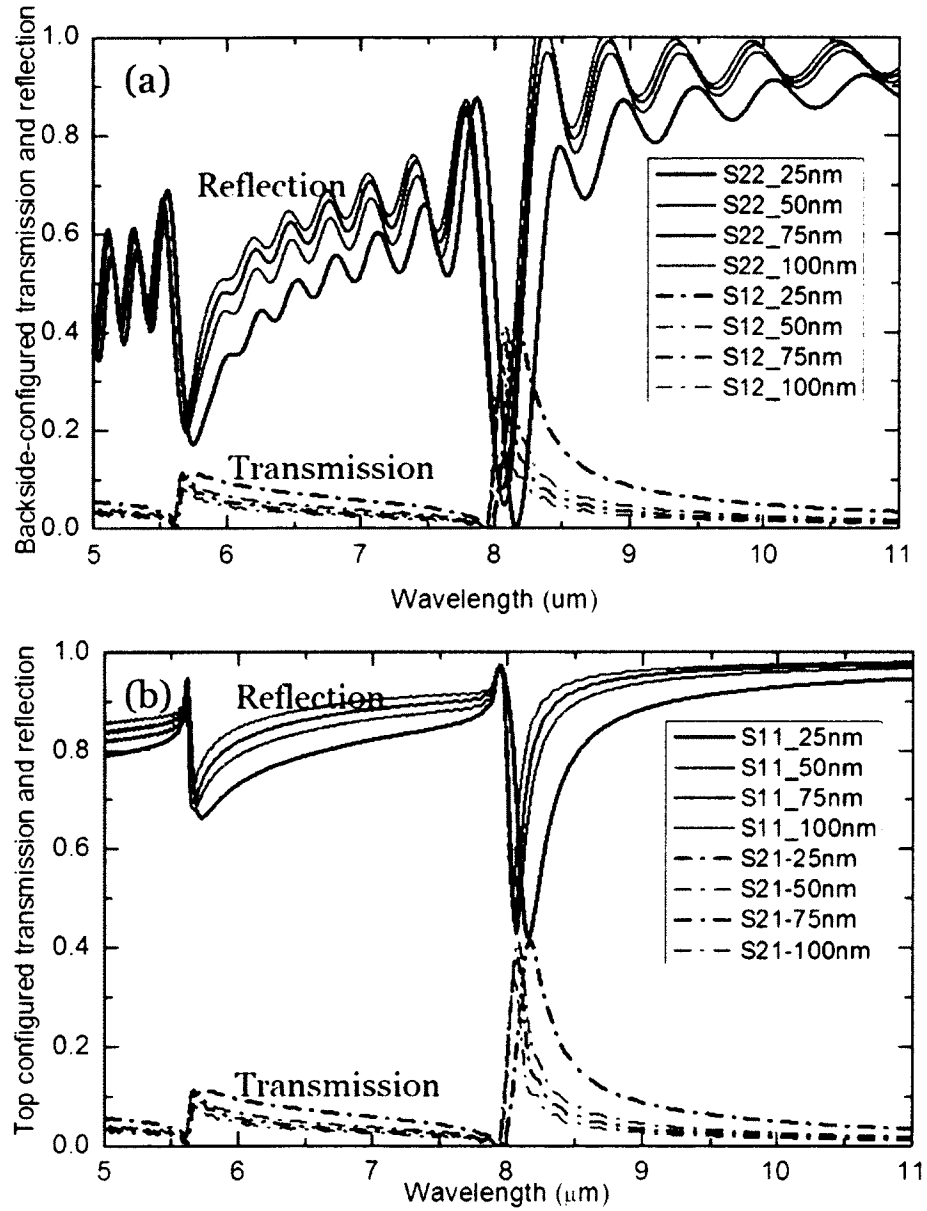
in Figure 67.

Figure 69 Simulated transmission (dashed lines) and reflection (solid lines) spectra. (a) backside-configured; (b) top-configured

Figure 70 shows the simulated transmission spectra of the 2DSHA plasmonic structures with different metal thickness versus frequency. It clearly show that the spectral width narrows as the metal thickness increases. In order to understand the spectral width narrowing effect, we analyze the loss of the plasmonic waves through the evanescent modes and its relationship with the metal thicknesses.
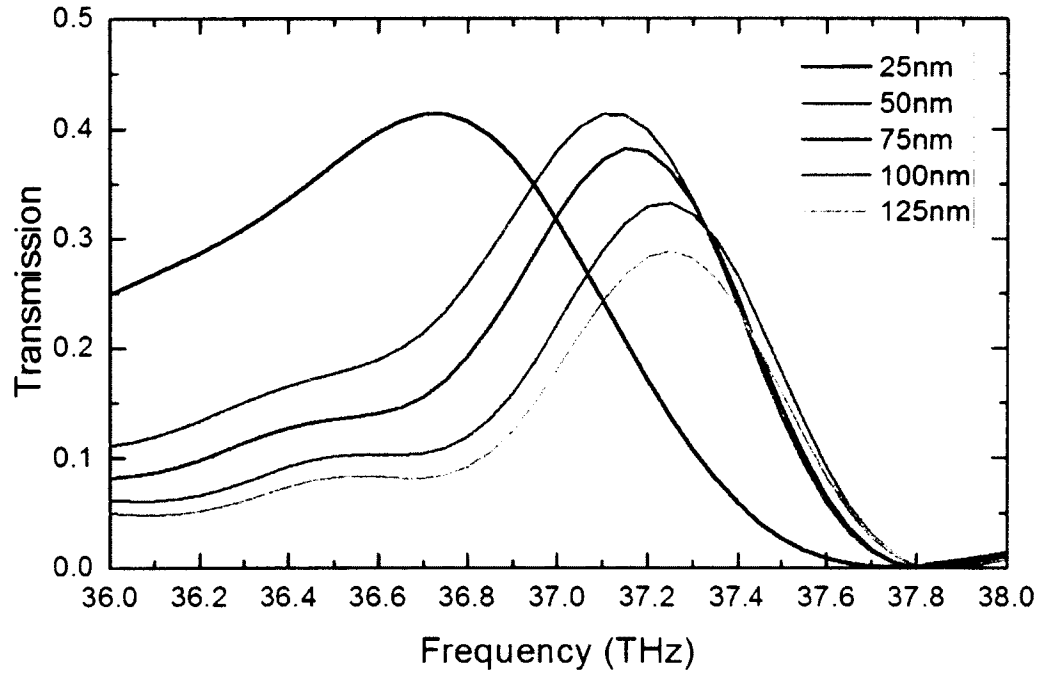
Figure 70 simulated transmission spectra of the 2DSHA plasmonic structures with different metal thickness versus frequency

If one ignores the other types of loss of the plasmonic waves (such as Ohmic and scattering loss), the loss of the plasmonic waves is through the radiation of the evanescent modes. The E field of the output light E_{out} can be written as:

$$E_{out} = TE_{in}e^{-|k_z|L},$$

(6.3)

where, E_{in} is the E field of the input light;

T is the transmission coefficient;

k_z is the z-component of the propagation constant;

L is the thickness of the metal;

$e^{-|k_z|L}$ term is the exponential decay of the evanescent modes.

The E_{out} can also be expressed using the lifetime of the plasmonic waves, i.e.

$$E_{out} = E_{in} e^{-t/\tau} ,$$
(6.4)

where, τ is the lifetime of the plasmonic waves.

Combining Eq. (1) and (2), one gets:

$$E_{in} e^{-t/\tau} = T E_{in} e^{-|k_z|L} ,$$
(6.5)

where, t is the time for the light travel through the cylindrical hole.

$$t = L / c ,$$
(6.6)

where, c is the speed of light.

Taking the natural logarithm of Eq. (6.5), one gets:

$$\frac{t}{\tau} = |k_z| L - \ln(T) .$$
(6.7)

Taking the t value in Eq. (6.6), one can obtain:

$$\frac{1}{\tau} = |k_z| c - \frac{c \ln(T)}{L} ,$$
(6.8)

Since the $2/\tau$ represents the spectral width (FWHM) in the frequency domain, the spectral width of the transmission v.s. 1/L should be a linear curve. Figure 71, shows the simulated spectral width v.s. 1/L curve, a very good linear relation between the spectral width (FWHM) and 1/L is obtained for the metal thickness of 50 nm, 75 nm, 100 nm, and 125 nm. This

validates the loss analysis. The spectral width of the 25 nm thick 2DSHA is larger than the

predication. This is possibly due to the thickness is less than the skin depth, and part of the

light can effectively go through the metal in addition to the transmission through the holes.

FWHM v.s. 1/L

$y = 15.643x + 0.4418$
$R^2 = 0.9919$
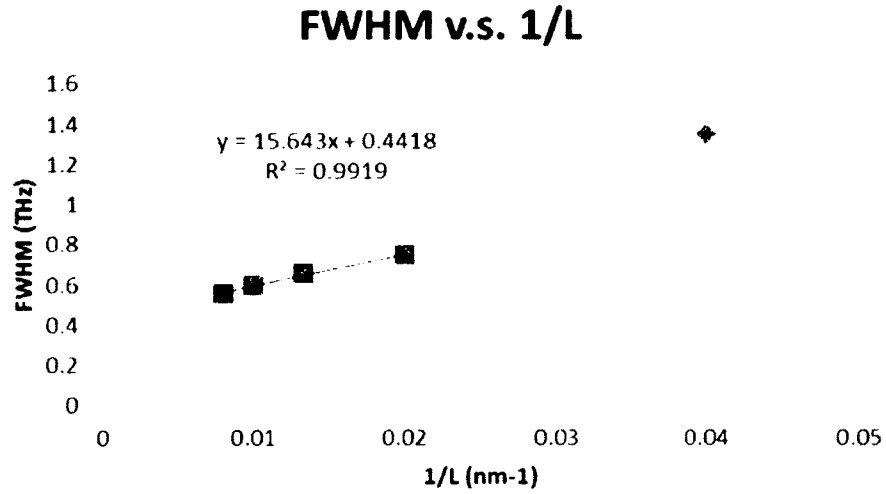
Figure 71 the simulated spectral width v.s. 1/L curve.

In conclusion, the metal thickness effect on the device performance enhancement was

examined from the perspectives of experiment, analysis and simulation, and compared

between the top- and backside- configured plasmonic structures. Clearly, the metal thickness

can dominate the enhancement factor and the spectral width significantly. Against the

top-configured plasmonic structures, the backside one with less reflection, higher plasmonic

excitation and thus higher enhancement factors was confirmed through the analysis and

simulation. A full theoretical analysis regarding as how the loss of the plasmonic waves is

obtained through the radiation of the evanescent modes and a highly linear relationship

between the spectral width and metal thickness is derived and further proved.

CHAPTER VII FUTURE WORK

The future work will primarily focus on the resonant cavity effect on the backside configured surface plasmonic structure on the QDIPs.

From the last project about metal thickness effect, as shown in Figure 67, although the enhancement factors are close for different metal thickness, the FTIR signals are dramatically different. Figure 72 shows the FTIR test results for the top- and backside-configured surface plasmonic structures with different metal thicknesses on the QDIPs and their references. The purple curve presents the backside-configured surface plasmonic FTIR signal, with the highest signal reaching to 0.07 (25nm metal thickness sample), while the lowest signal is 0.025 only (75nm metal thickness smaple). The green curve presents the top-configured surface plasmonic structure, which shows lower signal compared with the backside-configured curve. The blue and red curves in Figure 72 are the references. The QDIP with surface plasmonic structure FTIR signal magnitude depends on the structure, metal thickness and the reference signal. Since the structures are identical for all four samples, the causes of the distinctions can be driven by either the metal thicknes (25nm, 50nm, 75nm, and 100nm) or the substrate thickness (350um, 340um, 346um and 347um). However, for the reference QDIPs, the only difference is the substrate thickness, since there is no surface plasmonic structure on the top of Ref-QDIPs. The references show different FTIR signals which are dependent on the substrate thickness, or the resonant cavity effect.

Top and Backside configuration_25nm   (a)   Top and Backside-configuration_50nm   (b)

Top- and Backsid-configuration_75nm   (c)   Top- and Backside configuration_100nm   (d)
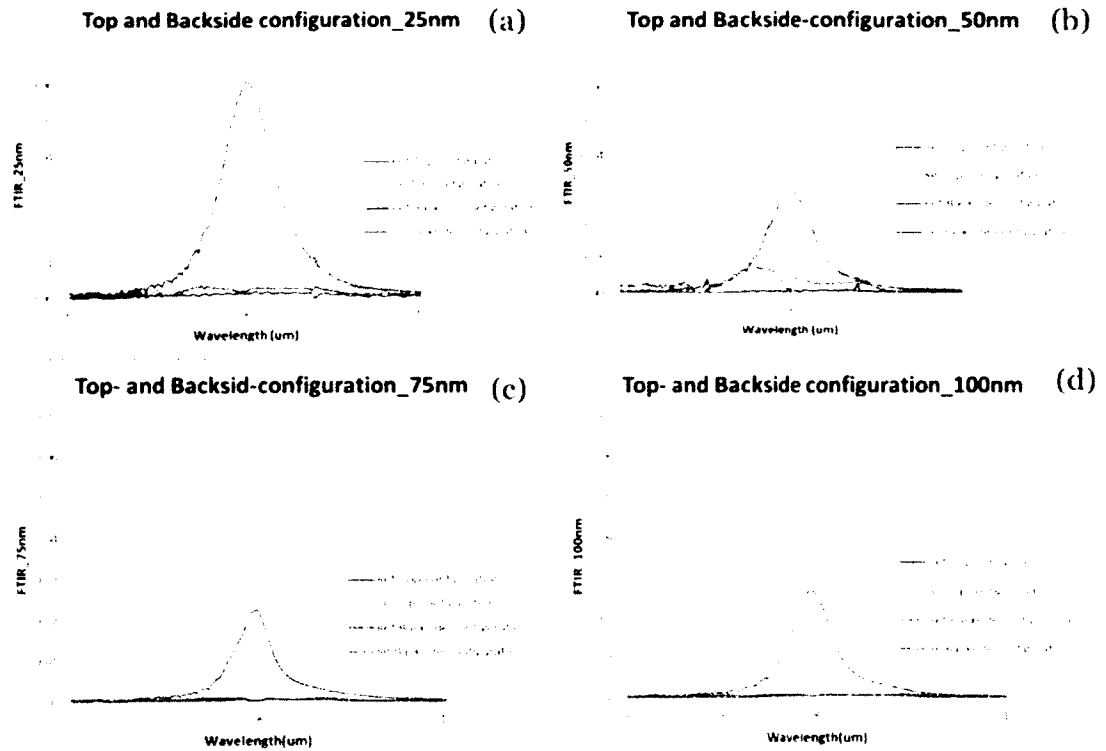
Figure 72 Top- and Backside-configured surface plasmonic structure with different metal thicknesses FTIR test results and their references. (a)SP metal thickness of 25nm; (b)SP metal thickness of 50nm; (c) SP metal thickness of   75nm; and (d)SP metal thickness of 100nm.

Figure 73 presents all the references FTIR signals for different metal thickness samples in top- and backside-configurations. Figure 73 (a) is top-configured references FTIR test results and Figure 73 (b) shows the backside-configured references FTIR test results. Apparently, signals vary by samples. The only differences for the samples are the substrate thickness, which implies that the resonant cavity can influence the sample signal. Therefore, proper design of the cavity length will give very high signal with surface plasmonic structures as shown in Figure 72, which is very important for many backside configured surface plamonic structure applications, such as FPAs.

All the references Top-configured FTIR   (a)
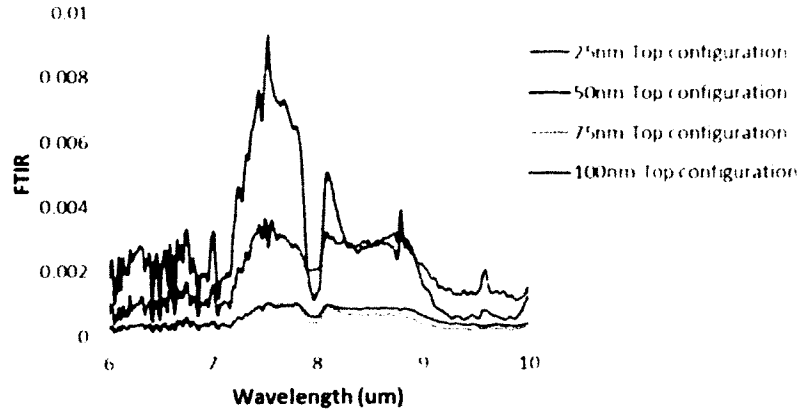
All the references Backside-configured FTIR   (b)
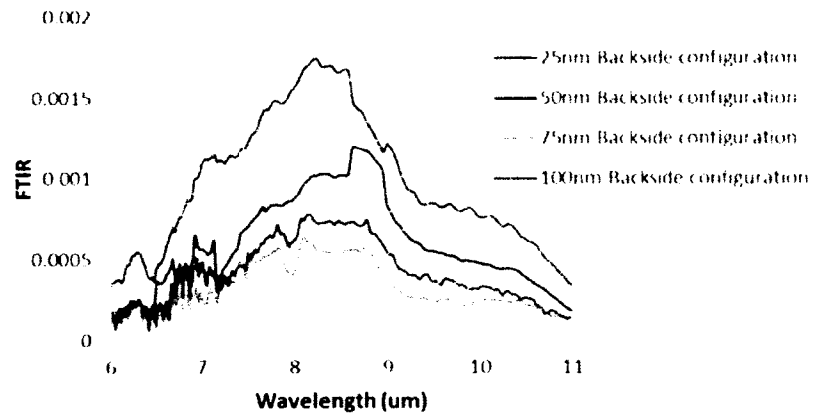
Figure 73 All the references with top- and backside-configuration FTIR test results. (a) Top-configured references FTIR; (b) Backside- configured references FTIR

Therefore, for future work, I suggest to perform investigation on the cavity effect and its roles in the QDIP performance and the plasmonic enhancement. To accurately measure the cavity effect, precisely control of the cavity length and the position of the active QD layers in the cavity are necessary. This can be done through incorporating the cavity design in the MBE

growth structure. The atomic layer accuracy of the MBE growth will allow the precise control of the cavity length and the location of the QD active layers in the cavity.

By optimizing the cavity length and the location of the QD active layers in the cavity, we can expect higher QDIP performance and larger plasmonic enhancement. Deeper understanding of the resonant cavity effect and its role in plasmonic enhancement can be obtained.

Reference:

1.   Herschel, W., *Experiments on the Refrangibility of the Invisible Rays of the Sun. By William Herschel, LL. DFRS.* Philosophical Transactions of the Royal Society of London, 1800. **90**: p. 284-292.
2.   Wright, H.C., *Infrared technique.* 1973. Oxford: Clarendon press.
3.   Bacon, C.P., Y. Mattley, and R. DeFrece, *Miniature spectroscopic instrumentation: Applications to biology and chemistry.* Review of Scientific Instruments, 2004. **75**(1): p. 1-16.
4.   Bagavathiappan, S., et al., *Infrared thermal imaging for detection of peripheral vascular disorders,* in *Journal of Medical Physics.* 2009.
5.   Wentworth, S.M. and D.P. Neikirk. *Far-infrared composite microbolometers.* in *Microwave Symposium Digest, 1990., IEEE MTT-S International.* 1990.
6.   Tribolet, P., et al., *Progress in HgCdTe homojunction infrared detectors.* Journal of Crystal Growth, 1998. **184–185**(0): p. 1262-1271.
7.   Destefanis, G.L., et al., *High-performance LWIR 256 x 256 HgCdTe focal plane array operating at 88 K.* 1997: p. 111-116.
8.   Biefeld, R.M., J.R. Wendt, and S.R. Kurtz, *Improving the performance of InAs1−xSbx/InSb infrared detectors grown by metalorganic chemical vapor deposition.* Journal of Crystal Growth, 1991. **107**(1–4): p. 836-839.
9.   Grein, C.H. and H. Ehrenreich, *Improvement of infrared detector performance in carrier depleted strained layer type II superlattices.* Journal of Applied Physics, 1997. **82**(12): p. 6365-6367.
10.   Levine, B.F., *Quantum well infrared photodetectors.* Journal of Applied Physics, 1993. **74**(8): p. R1-R81.
11.   Chen, C., et al., *Two-color corrugated quantum-well infrared photodetector for remote temperature sensing.* Applied physics letters, 1998. **72**(1): p. 7-9.

12. Gunapala, S. and K. Bandara, *Recent developments in quantum-well infrared photodetectors.* Thin Films, 1995. **21**: p. 113-237.

13. Martyniuk, P. and A. Rogalski, *Quantum-dot infrared photodetectors: Status and outlook.* Progress in Quantum Electronics, 2008. **32**(3): p. 89-120.

14. Bhattacharya, P., et al., *Quantum dot infrared detectors and sources.* International journal of high speed electronics and systems, 2002. **12**(04): p. 969-994.

15. Gunapala, S.D., et al., *640× 486 long-wavelength two-color GaAs/AlGaAs quantum well infrared photodetector (QWIP) focal plane array camera.* Electron Devices, IEEE Transactions on, 2000. **47**(5): p. 963-971.

16. Rogalski, A., *Outlook on quantum dot infrared photodetectors.* Optical Memory and Neural Networks, 2009. **18**(3): p. 234-252.

17. Sattler, K.D., *Handbook of Nanophysics: Functional Nanomaterials.* 2010: CRC Press.

18. Perera, A., et al., *GaAs/AlGaAs quantum well photodetectors with a cutoff wavelength at 28 μ m.* Applied physics letters, 1998. **72**(13): p. 1596-1598.

19. Meisner, M.J., J. Vaillancourt, and X. Lu, *Voltage-tunable dual-band InAs quantum-dot infrared photodetectors based on InAs quantum dots with different capping layers.* Semiconductor Science and Technology, 2008. **23**(9): p. 095016.

20. Lu, X., J. Vaillancourt, and M.J. Meisner. *A voltage-tunable multiband quantum dot infrared focal plane array with high photodetectivity.* in *SPIE Defense and Security Symposium.* 2008: International Society for Optics and Photonics.

21. Lu, X., J. Vaillancourt, and M.J. Meisner, *Temperature-dependent photoresponsivity and high-temperature (190 K) operation of a quantum dot infrared photodetector.* Applied physics letters, 2007. **91**: p. 051115.

22. Jiang, L., et al. *An In0. 6Ga0. 4As/GaAs quantum dot infrared photodetector with operating temperature up to 260K.* in *AeroSense 2003.* 2003: International Society for Optics and Photonics.

23. Chakrabarti, S., et al., *High-temperature operation of InAs-GaAs quantum-dot infrared photodetectors with large responsivity and detectivity.* Photonics Technology Letters, IEEE, 2004. **16**(5): p. 1361-1363.

24. Lim, H., et al., *High-performance InAs quantum-dot infrared photodetectors grown on InP substrate operating at room temperature.* Applied physics letters, 2007. **90**(13): p. 131112-131112-3.

25. Vaillancourt, J., et al. *A LWIR quantum dot infrared photodetector working at 298K.* in *OPTO.* 2010: International Society for Optics and Photonics.

26. Ritchie, R., *Plasma losses by fast electrons in thin films.* Physical Review, 1957. **106**(5): p. 874.

27. Ebbesen, T.W., et al., *Extraordinary optical transmission through sub-wavelength hole arrays.* Nature, 1998. **391**(6668): p. 667-669.

28. Atwater, H.A. and A. Polman, *Plasmonics for improved photovoltaic devices.* Nature materials, 2010. **9**(3): p. 205-213.

29. Ghaemi, H., et al., *Surface plasmons enhance optical transmission through subwavelength holes.* Physical Review B, 1998. **58**(11): p. 6779.

30. Chergui, M., A. Melikyan, and H. Minassian. *Calculation of Surface Plasmon Frequencies of Two, Three, and Four Strongly Interacting Nanospheres.* The Journal of Physical Chemistry C, 2009. **113**(16): p. 6463-6471.

31. Liu, R., *Evanescent waveguide modes in subwavelength hole arrays and their role in enhancing the performance of quantum dot infrared photodetectors.* 2011, University of Massachusetts Lowell: United States -- Massachusetts. p. 94.

32. Shalabney, A. and I. Abdulhalim, *Electromagnetic fields distribution in multilayer thin film structures and the origin of sensitivity enhancement in surface plasmon resonance sensors.* Sensors and Actuators A: Physical, 2010. **159**(1): p. 24-32.

33. Hellstrom, S., et al., *Increased photocurrent in quantum dot infrared photodetector by subwavelength hole array in metal thin film.* Applied physics letters, 2010. **96**(23): p. 231110-231110-3.

34. Chang, C.-C., et al., *A surface plasmon enhanced infrared photodetector based on InAs quantum dots.* Nano letters, 2010. **10**(5): p. 1704-1709.

35. Liu, R., et al., *Optimizing light absorption in quantum dot infrared photodetectors by tuning surface confinement of surface plasmonic waves.* Journal of Physics D: Applied Physics, 2013. **46**(1): p. 015102.

36. Vasinajindakaw, P., et al., *A Fano-type interference enhanced quantum dot infrared photodetector.* Applied physics letters, 2011. **98**(21): p. 211111-211111-3.

37. Vasinajindakaw, P., et al., *Surface plasmonic enhanced polarimetric longwave infrared photodetection with band pass spectral filtering.* Semiconductor Science and Technology, 2012. **27**(6): p. 65005-65009.

38. Bethe, H., *Theory of diffraction by small holes.* Physical Review, 1944. **66**(7-8): p. 163-182.

39. Krishnan, A., et al., *Evanescently coupled resonance in surface plasmon enhanced transmission.* Optics communications, 2001. **200**(1): p. 1-7.

40. Lee, S.J., et al., *A monolithically integrated plasmonic infrared quantum dot camera.* Nat Commun, 2011. **2**: p. 286.

41. Vasinajindakaw, P., *Surface plasmon enhanced quantum dot infrared photodetector.* 2012, University of Massachusetts Lowell: United States -- Massachusetts. p. 112.

42. Lee, S., S. Krishna, and S. Brueck, *Quantum dot infrared photodetector enhanced by surface plasma wave excitation.* Opt. Express, 2009. **17**(25): p. 23160-23168.

43. Lee, S., S. Krishna, and S. Brueck, *Light direction-dependent plasmonic enhancement in quantum dot infrared photodetectors.* Applied physics letters, 2010. **97**(2): p. 021112-021112-3.

44. Snitzer, E., *Cylindrical dielectric waveguide modes.* JOSA, 1961. **51**(5): p. 491-498.